Improving Flow Matching by Aligning Flow Divergence

Yuhao Huang [1 2] **Taos Transue** [1 2] **Shih-Hsin Wang** [1 2] **William Feldman** [1] **Hong Zhang** [3] **Bao Wang** [1 2]

Abstract

Conditional flow matching (CFM) stands out as an efficient, simulation-free approach for training flow-based generative models, achieving remarkable performance for data generation. However, CFM is insufficient to ensure accuracy in learning probability paths. In this paper, we introduce a new partial differential equation characterization for the error between the learned and exact probability paths, along with its solution. We show that the total variation gap between the two probability paths is bounded above by a combination of the CFM loss and an associated divergence loss. This theoretical insight leads to the design of a new objective function that simultaneously matches the flow and its divergence. Our new approach improves the performance of the flow-based generative model by a noticeable margin without sacrificing generation efficiency. We showcase the advantages of this enhanced training approach over CFM on several important benchmark tasks, including generative modeling for dynamical systems, DNA sequences, and videos. Code is available at Utah-Math-Data-Science.

1. Introduction

Flow matching (FM) – leveraging a neural network to learn a predefined vector field mapping between noise and data samples – has emerged as an efficient simulation-free training approach for flow-based generative models (FGMs), achieving remarkable stability, computational efficiency, and flexibility for generative modeling (Lipman et al., 2023; Albergo & Vanden-Eijnden, 2023; Liu et al., 2023). Compared to the classical likelihood-based approaches for training FGMs, e.g., (Chen et al., 2018; Grathwohl et al., 2018), FM circumvents computationally expensive sample simulations to estimate gradients or densities. The celebrated diffusion models (DMs) with variance preserving (VP) or variance exploding (VE) stochastic differential equations (SDEs) (Song et al., 2020) can be viewed as special FGMs with diffusion paths (c.f. Section 2). Furthermore, FM excels in generative modeling on non-Euclidean spaces, broadening its scientific applications (Chen & Lipman, 2024; Jing et al., 2023; Bose et al., 2024; Yim et al., 2024; Stark et al., 2024).

At the core of FM is the idea of regressing a vector field that interpolates between the prior noise distribution $q(\boldsymbol{x})$ – typically the standard Gaussian – and the data distribution $p(\boldsymbol{x})$. Specifically, we aim to regress the vector field $\boldsymbol{u}_t(\boldsymbol{x})$ that guides the probability flow $p_t(\boldsymbol{x})$ interpolating between an easy-to-sample noise and the data distributions, i.e., $p_0 = q$ and $p_1 \approx p$. The relationship between $\boldsymbol{u}_t$ and p_t is formalized by the following continuity equation (Villani et al., 2009):

$$\frac{\partial p_t(\boldsymbol{x})}{\partial t} + \nabla \cdot (p_t(\boldsymbol{x})\boldsymbol{u}_t(\boldsymbol{x})) = 0.$$

FM approximates $\boldsymbol{u}_t$ using a neural network-parameterized vector field $\boldsymbol{v}_t(\boldsymbol{x}, \theta)$, seeking to minimize the FM loss:

$$\mathcal{L}_{\mathrm{FM}}(\theta) := \mathbb{E}_{t,p_t(\boldsymbol{x})}\left[\left\|\boldsymbol{v}_t(\boldsymbol{x},\theta) - \boldsymbol{u}_t(\boldsymbol{x})\right\|^2\right], \qquad (1)$$

where $t \sim U[0,1]$ follows a uniform distribution over the unit time interval $[0,1]$.

However, equation (1) is intractable as $\boldsymbol{u}_t(\boldsymbol{x})$ is unavailable. To address this, an alternative simulation-free method, known as conditional flow matching (CFM) (Lipman et al., 2023; Albergo & Vanden-Eijnden, 2023), is employed. In CFM, $\boldsymbol{v}_t(\boldsymbol{x}, \theta)$ is trained by regressing against a predefined conditional vector field on a per-sample basis, ensuring both computational efficiency and accuracy. Concretely, for any data sample $\boldsymbol{x}_1 \sim p(\boldsymbol{x})$, we can define a conditional probability path $p_t(\boldsymbol{x}|\boldsymbol{x}_1)$ for $t \in [0,1]$ satisfying $p_0(\boldsymbol{x}|\boldsymbol{x}_1) = q(\boldsymbol{x})$ and $p_1(\boldsymbol{x}|\boldsymbol{x}_1) \approx \delta(\boldsymbol{x} - \boldsymbol{x}_1)$, and define the associated conditional vector field $\boldsymbol{u}_t(\boldsymbol{x}|\boldsymbol{x}_1)$; see Section 2 for a review on several common designs of conditional probability paths. Once the conditional probability paths are defined, the marginal probability path $p_t(\boldsymbol{x})$ is given by:

$$p_t(\boldsymbol{x}) := \int p_t(\boldsymbol{x}|\boldsymbol{x}_1)p(\boldsymbol{x}_1)d\boldsymbol{x}_1.$$

[1]Department of Mathematics, University of Utah, Salt Lake City, UT, USA [2]Scientific Computing and Imaging (SCI) Institute, Salt Lake City, UT, USA [3]Mathematics and Computer Science Division, 240 Argonne National Laboratory, Lemont, IL, USA. Correspondence to: Bao Wang <wangbaonj@gmail.com>.

Proceedings of the 42nd International Conference on Machine Learning, Vancouver, Canada. PMLR 267, 2025. Copyright 2025 by the author(s).

Similarly, the marginal vector field is defined as:

$$\boldsymbol{u}_t(\boldsymbol{x}) := \int \boldsymbol{u}_t(\boldsymbol{x}|\boldsymbol{x}_1)\frac{p_t(\boldsymbol{x}|\boldsymbol{x}_1)p(\boldsymbol{x}_1)}{p_t(\boldsymbol{x})}d\boldsymbol{x}_1.$$

With these relations in mind, CFM regresses $\boldsymbol{v}_t(\boldsymbol{x},\theta)$ against $\boldsymbol{u}_t(\boldsymbol{x}|\boldsymbol{x}_1)$ by minimizing the following CFM loss:

$$\mathcal{L}_{\mathrm{CFM}}(\theta) := \mathbb{E}_{t,p(\boldsymbol{x}_1),p_t(\boldsymbol{x}|\boldsymbol{x}_1)}\left[\left\|\boldsymbol{v}_t(\boldsymbol{x},\theta) - \boldsymbol{u}_t(\boldsymbol{x}|\boldsymbol{x}_1)\right\|^2\right]. \tag{2}$$

It has been shown that the CFM loss is identical to the FM loss up to a constant that is independent of θ (c.f. (Lipman et al., 2023)[Theorem 2]). Therefore, minimizing $\mathcal{L}_{\mathrm{CFM}}(\theta)$ enables $\boldsymbol{v}_t(\boldsymbol{x},\theta)$ to be an unbiased estimate for the marginal vector field $\boldsymbol{u}_t(\boldsymbol{x})$.

While CFM enables $\boldsymbol{v}_t(\boldsymbol{x},\theta)$ to efficiently approximate $\boldsymbol{u}_t(\boldsymbol{x})$, we observe that their divergence gap[1] $|\nabla\cdot\boldsymbol{v}_t(\boldsymbol{x},\theta) - \nabla\cdot\boldsymbol{u}_t(\boldsymbol{x})|$ can be substantial, resulting in significant errors in learning the probability path and estimating sample likelihood. Figure 1 highlights the challenges in learning a Gaussian mixture distribution using CFM. The full experimental setup for this result is provided in Section 3. Additionally, we will prove the existence of an intrinsic bottleneck of FM. This underscores the importance of improving FM for generative modeling, especially for tasks requiring accurate sample likelihood estimation. Indeed, such tasks are ubiquitous in climate modeling (Finzi et al., 2023; Wan et al., 2023; Li et al., 2024), molecular dynamics simulation (Petersen et al.), cyber-physical systems (Delecki et al., 2024), and beyond (Hua et al., 2024).

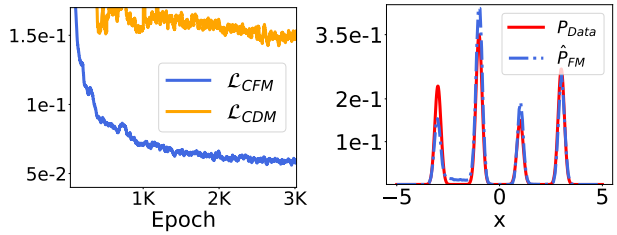

Figure 1. Experiments of training an FM model using CFM for sampling the 1D Gaussian mixture distribution in equation (18). The left panel shows that the conditional divergence loss $\mathcal{L}_{\mathrm{CDM}}$ in equation (14) is much larger than the CFM loss $\mathcal{L}_{\mathrm{CFM}}$, and the right panel shows the significant gap between the exact distribution (p_{Data}) and the distribution learned through FM ($\hat{p}_{\mathrm{FM}}$).

1.1. Our Contribution

We summarize our key contributions as follows:

- We characterize the error between the exact ($p_t(\boldsymbol{x})$) and learned ($\hat{p}_t(\boldsymbol{x})$) probability paths using a partial differential equation (PDE); see Proposition 3.1. This new error characterization describes how the error propagates over time, allowing us to derive a total variation (TV)-based error bound between the two probability paths; see Corollary 3.2 and Theorem 3.3. These theoretical results underscore the importance of controlling the divergence gap to enhance the accuracy in learning $\hat{p}_t(\boldsymbol{x})$.
- Informed by our established TV error bound, we develop a new training objective by combining the CFM loss with the divergence gap. However, directly minimizing the divergence gap is intractable since the divergence of the marginal vector field is unavailable. To address this issue, we propose a conditional divergence gap – an upper bound for the unconditional divergence gap. We refer to this new training objective as flow and divergence matching (FDM); see Section 4 for details.
- We validate the performance of FDM across several benchmark tasks, including synthetic density estimation, trajectory sampling for dynamical systems, video generation, and DNA sequence generation. Our numerical results, presented in Section 5, show that our proposed FDM can improve likelihood estimation and enhance sample generation by a remarkable margin over CFM.

1.2. Some Additional Related Works

The Kullback-Leibler (KL) divergence between the exact and learned distributions has been studied for DMs (c.f. (Song et al., 2021; Lu et al., 2022; Lai et al., 2023)) and FM (c.f. (Albergo et al., 2023)) with ODE flows, where it was observed that the FM loss in equation (1) alone is insufficient for minimizing the KL divergence between two probability paths, and the KL divergence bound depends on higher-order score functions.

Several works have explored improving training DMs with higher-order score matching. For instance, Meng et al. (2021) have proposed high-order denoising score matching leveraging Tweedie's formula (Robbins, 1992; Efron, 2011) to provide a more accurate local approximation of the data density (e.g., its curvature). We notice that the trace of the second-order score matching proposed in (Meng et al., 2021) resonates with the idea of our proposed FDM in the context of DMs. Additionally, inspired by the KL divergence bound, high-order score matching – matching up to third-order score – has been used to improve likelihood estimation for training DMs (Lu et al., 2022). Nevertheless, these higher-order score-matching methods are significantly more computationally expensive than our proposed FDM.

Enforcing the continuity equation for flow dynamics is another related work that has been studied in the context of DMs. In particular, Lai et al. (2023) shows that the score function satisfies a Fokker-Planck equation (FPE) and directly penalizes the loss function with the error from plug-

[1] Here, we use the absolute value notation since the divergence of the vector field is a scalar.

ging the learned score function into the score FPE. To the best of our knowledge, developing a PDE characterization of the error between the exact and learned probability paths and bounding their TV gap using only the vector field and its divergence have not been considered in the literature.

1.3. Organization

We organize this paper as follows. We provide a brief review of FM in Section 2. In Section 3, we present our theoretical analysis of the gap between the exact and learned probability paths, accompanied by illustrative numerical evidence. We present FDM to improve training FGMs in Section 4. We verify the advantages of FDM over FM using a few representative benchmark tasks in Section 5. Technical proofs, additional experimental details, and experimental results are provided in the appendix.

2. Flow Matching

In this section, we provide a brief review of FM and prevalent designs of conditional probability paths. A vector field $\boldsymbol{u}_t : [0,1] \times \mathbb{R}^d \to \mathbb{R}^d$ defines a flow $\boldsymbol{\psi}_t : [0,1] \times \mathbb{R}^d \to \mathbb{R}^d$ through the following ODE:

$$\frac{d}{dt}\boldsymbol{\psi}_t(\boldsymbol{x}) = \boldsymbol{u}_t(\boldsymbol{\psi}_t(\boldsymbol{x})), \tag{3}$$

with the initial condition $\boldsymbol{\psi}_0(\boldsymbol{x}) = \boldsymbol{x}$. FGMs, e.g., continuous normalizing flows (Grathwohl et al., 2018), map a prior noise distribution $p_0 = q$ to data distribution $p_1 \approx p$ via the following map:

$$p_t(\boldsymbol{x}) = p_0(\boldsymbol{\psi}_t^{-1}(\boldsymbol{x}))\det\Big[\frac{\partial \boldsymbol{\psi}_t^{-1}}{\partial \boldsymbol{x}}(\boldsymbol{x})\Big],\ \forall \boldsymbol{x} \in p_0.$$

For a given sample $\boldsymbol{x}_1 \sim p$, FM defines a conditional probability path satisfying $p_0(\boldsymbol{x}|\boldsymbol{x}_1) = q(\boldsymbol{x})$ and $p_1(\boldsymbol{x}|\boldsymbol{x}_1) \approx \delta(\boldsymbol{x} - \boldsymbol{x}_1)$ – the Dirac-delta distribution centered at $\boldsymbol{x}_1$, and the corresponding conditional vector field $\boldsymbol{u}_t(\boldsymbol{x}|\boldsymbol{x}_1)$. Then FM regresses a neural network-parameterized unconditional vector field $\boldsymbol{v}_t(\boldsymbol{x}, \theta)$ by minimizing CFM in equation (2).

A prevalent choice for $p_t(\boldsymbol{x}|\boldsymbol{x}_t)$ is the Gaussian conditional probability path given by

$$p_t(\boldsymbol{x}|\boldsymbol{x}_1) = \mathcal{N}(\boldsymbol{x}|\boldsymbol{\mu}_t(\boldsymbol{x}_1), \sigma_t(\boldsymbol{x}_1)^2\boldsymbol{I}),$$

with $\boldsymbol{\mu}_0(\boldsymbol{x}_1) = \boldsymbol{0}$ and $\sigma_0(\boldsymbol{x}_1) = 1$. Moreover, $\boldsymbol{\mu}_1(\boldsymbol{x}_1) = \boldsymbol{x}_1$ and $\sigma_1(\boldsymbol{x}_1)$ is a small number so that $p_1(\boldsymbol{x}|\boldsymbol{x}_1) \approx \delta(\boldsymbol{x} - \boldsymbol{x}_1)$. Some celebrated DMs can be interpreted as FM models with Gaussian conditional probability paths. In particular, the generation process of the DM with VE SDE (Song et al., 2020) has the conditional probability path:

$$p_t(\boldsymbol{x}|\boldsymbol{x}_1) = \mathcal{N}(\boldsymbol{x}|\boldsymbol{x}_1, \sigma_{1-t}^2\boldsymbol{I}),$$

where σ_t is an increasing function satisfying $\sigma_0 = 0$ and $\sigma_1 \gg 1$. The corresponding conditional vector field is given by

$$\boldsymbol{u}_t(\boldsymbol{x}|\boldsymbol{x}_1) = -\frac{\sigma'_{1-t}}{\sigma_{1-t}}(\boldsymbol{x} - \boldsymbol{x}_1).$$

where σ'_{1-t} denote the derivative of the function. Likewise, the VP SDE (Song et al., 2020) has the following conditional probability path:

$$p_t(\boldsymbol{x}|\boldsymbol{x}_1) = \mathcal{N}(\boldsymbol{x}|\alpha_{1-t}\boldsymbol{x}_1, (1 - \alpha_{1-t}^2)\boldsymbol{I}),$$

where $\alpha_t = e^{-\frac{1}{2}T(t)}$ and $T(t) = \int_0^t \beta(s)ds$ with $\beta(s)$ being the noise scale function. The corresponding conditional vector field is

$$\boldsymbol{u}_t(\boldsymbol{x}|\boldsymbol{x}_1) = \frac{\alpha'_{1-t}}{1 - \alpha_{1-t}^2}(\alpha_{1-t}\boldsymbol{x} - \boldsymbol{x}_1).$$

Besides diffusion paths, the optimal transport (OT) path is another remarkable choice (Lipman et al., 2023). OT path uses the Gaussian conditional probability path with

$$\boldsymbol{\mu}_t(\boldsymbol{x}) = t\boldsymbol{x}_1, \text{ and } \sigma_t(\boldsymbol{x}) = 1 - (1 - \sigma_{\min})t.$$

The corresponding conditional vector field is given by

$$\boldsymbol{u}_t(\boldsymbol{x}|\boldsymbol{x}_1) = \frac{\boldsymbol{x}_1 - (1 - \sigma_{\min})\boldsymbol{x}}{1 - (1 - \sigma_{\min})t}.$$

3. Error Analysis for Probability Paths

In this section, we analyze the error between the two probability paths associated with the exact and learned vector fields, respectively. Specifically, we show that this error satisfies a PDE similar to the original continuity equation, but with an additional forcing term. Using Duhamel's principle (Seis, 2017), we reveal that this forcing term directly governs the magnitude of the error. Details of the omitted proofs, along with the common assumptions employed by (Lu et al., 2022; Lipman et al., 2023; Albergo et al., 2023) and adopted in our theoretical results, are provided in Appendix A.

3.1. PDE for the Error Between Probability Flows

Recall that the marginal probability path $p_t(\boldsymbol{x})$ and the marginal vector field $\boldsymbol{u}_t(\boldsymbol{x})$ satisfy the following continuity equation (Villani et al., 2009):

$$\frac{\partial p_t(\boldsymbol{x})}{\partial t} + \nabla \cdot (p_t(\boldsymbol{x})\boldsymbol{u}_t(\boldsymbol{x})) = 0. \tag{4}$$

We can rewrite the continuity equation into the following non-conservative form:

$$\frac{\partial p_t(\boldsymbol{x})}{\partial t} = -(\nabla \cdot \boldsymbol{u}_t(\boldsymbol{x}))p_t(\boldsymbol{x}) - \boldsymbol{u}_t(\boldsymbol{x}) \cdot \nabla p_t(\boldsymbol{x}). \tag{5}$$

Similarly, consider the probability path $\hat{p}_t(\boldsymbol{x})$ associated with the neural network-parametrized vector field $\boldsymbol{v}_t(\boldsymbol{x}, \theta)$. This probability path satisfies the following continuity equation, which has the same initial condition as the ground truth equation (5), i.e., $p_0 = \hat{p}_0$:

$$\frac{\partial \hat{p}_t(\boldsymbol{x})}{\partial t} = -(\nabla \cdot \boldsymbol{v}_t(\boldsymbol{x}, \theta))\hat{p}_t(\boldsymbol{x}) - \boldsymbol{v}_t(\boldsymbol{x}, \theta) \cdot \nabla \hat{p}_t(\boldsymbol{x}). \quad (6)$$

We now introduce the error term $\epsilon_t(\boldsymbol{x}) \coloneqq p_t(\boldsymbol{x}) - \hat{p}_t(\boldsymbol{x})$. The following proposition shows that ϵ_t satisfies a PDE similar to equation (4), but with an additional forcing term that reflects the discrepancy between the vector fields $\boldsymbol{u}_t$ and $\boldsymbol{v}_t$.

Proposition 3.1. *$\epsilon_t \coloneqq p_t - \hat{p}_t$ satisfies the following PDE:*

$$\begin{cases} \partial_t \epsilon_t + \nabla \cdot \big(\epsilon_t \boldsymbol{v}_t\big) = L_t, \\ \epsilon_0(\boldsymbol{x}) = 0, \end{cases} \quad (7)$$

where

$$L_t = -p_t \Big[\nabla \cdot (\boldsymbol{u}_t - \boldsymbol{v}_t) + (\boldsymbol{u}_t - \boldsymbol{v}_t) \cdot \nabla \log p_t\Big]. \quad (8)$$

3.2. Error Bound for Probability Paths

FM aims to minimize the discrepancy between p_t and $\hat{p}_t$ by reducing the difference between their associated vector fields, $\boldsymbol{u}_t(\boldsymbol{x})$ and $\boldsymbol{v}_t(\boldsymbol{x}, \theta)$, through minimizing the CFM loss equation (2). However, Proposition 3.1 highlights that the error dynamics are not only influenced by $\boldsymbol{u}_t - \boldsymbol{v}_t$ but also by $\nabla \cdot (\boldsymbol{u}_t - \boldsymbol{v}_t)$, as both terms contribute to the forcing term in equation (7). To formalize this observation, we solve ϵ_t using Duhamel's formula (Seis, 2017). In particular, we have the following result:

Corollary 3.2. *For any $t \in [0, 1]$, the error ϵ_t satisfies*

$$\epsilon_t(\phi_t(\boldsymbol{x})) \cdot \det \nabla \phi_t(\boldsymbol{x}) = -\int_0^t L_s(\phi_s(\boldsymbol{x})) \cdot \det \nabla \phi_s(\boldsymbol{x}) ds,$$

where $\phi_t(\boldsymbol{x})$ is the flow induced by the vector field $\boldsymbol{v}_t(\boldsymbol{x})$ in a similar way as that in equation (3), $\det \nabla \phi_t(\boldsymbol{x})$ denotes the determinant of the Jacobian matrix $\nabla \phi_t(\boldsymbol{x})$, and L_s is defined in Proposition 3.1.

Corollary 3.2 suggests that minimizing the divergence gap is as important as reducing the vector field discrepancy in order to learn an accurate probability path.

To quantify the error ϵ_t, we consider the following TV distance between p_t and $\hat{p}_t$:

$$\begin{aligned} \mathrm{TV}(p_t, \hat{p}_t) &\coloneqq \frac{1}{2} \int \big|p_t(\boldsymbol{x}) - \hat{p}_t(\boldsymbol{x})\big| \, d\boldsymbol{x} \\ &= \frac{1}{2} \int \big|\epsilon_t(\boldsymbol{x})\big| \, d\boldsymbol{x}. \end{aligned} \quad (9)$$

Motivated by the error-related identity in Corollary 3.2 and the form of L_t in equation (8), we introduce an additional term as follows:

$$\mathcal{L}_{\mathrm{DM}}(\theta) \coloneqq \mathbb{E}_{t, p_t(\boldsymbol{x})} \Bigg[\Big|\nabla \cdot (\boldsymbol{u}_t - \boldsymbol{v}_t) + (\boldsymbol{u}_t - \boldsymbol{v}_t) \cdot \nabla \log p_t\Big|\Bigg]. \quad (10)$$

The following Theorem establishes an upper bound for the error term $\mathrm{TV}(p_t, \hat{p}_t)$ in terms of $\mathcal{L}_{\mathrm{DM}}(\theta)$.

Theorem 3.3. *Under some common mild assumptions adopted in (Lu et al., 2022; Lipman et al., 2023; Albergo et al., 2023), the following inequality holds for any $t \in [0, 1]$:*

$$\mathrm{TV}(p_t, \hat{p}_t) \leq \frac{1}{2} \mathcal{L}_{\mathrm{DM}}(\theta). \quad (11)$$

Specifically, $p_t(\boldsymbol{x}) = \hat{p}_t(\boldsymbol{x})$ when both $\mathcal{L}_{\mathrm{DM}}$ is zero.

4. Conditional Divergence Matching

In the previous section, we have highlighted the importance of matching the divergence between $\boldsymbol{u}_t$ and $\boldsymbol{v}_t$ beyond matching the vector fields themselves. However, directly minimizing the divergence loss presents a computational challenge, as computing the divergence of the exact unconditional vector field is intractable. To address this issue, we will leverage a similar idea to the conditional flow matching to address the computational issue.

We start by deriving the conditional version of $\mathcal{L}_{\mathrm{DM}}(\theta)$. We recall the following conditional form of the continuity equation from (Lipman et al., 2023):

$$\partial_t p_t(\boldsymbol{x}|\boldsymbol{x}_1) = \nabla \cdot \big(p_t(\boldsymbol{x}|\boldsymbol{x}_1) \boldsymbol{u}_t(\boldsymbol{x}|\boldsymbol{x}_1)\big), \quad (12)$$

which relates the evolution of the conditional probability density $p_t(\boldsymbol{x}|\boldsymbol{x}_1)$ to the divergence of $p_t(\boldsymbol{x}|\boldsymbol{x}_1)\boldsymbol{u}_t(\boldsymbol{x}|\boldsymbol{x}_1)$. By integrating over the conditioning variable $\boldsymbol{x}_1$ and applying the continuity equation (4), we obtain the following connection between the conditional divergence and unconditional divergence:

$$\begin{aligned} &\nabla \cdot \big(p_t(\boldsymbol{x}) \boldsymbol{u}_t(\boldsymbol{x})\big) \\ =&\partial_t p_t(\boldsymbol{x}) \\ =&\int \partial_t p_t(\boldsymbol{x}|\boldsymbol{x}_1) p(\boldsymbol{x}_1) \, d\boldsymbol{x}_1 \\ =&\int \nabla \cdot \big(p_t(\boldsymbol{x}|\boldsymbol{x}_1) \boldsymbol{u}_t(\boldsymbol{x}|\boldsymbol{x}_1)\big) p(\boldsymbol{x}_1) \, d\boldsymbol{x}_1. \end{aligned} \quad (13)$$

Furthermore, we observe the following identity:

$$\begin{aligned} &p_t \Big[\nabla \cdot (\boldsymbol{u}_t - \boldsymbol{v}_t) + (\boldsymbol{u}_t - \boldsymbol{v}_t) \cdot \nabla \log p_t\Big] \\ =&\nabla \cdot (p_t \boldsymbol{u}_t) - \nabla \cdot (p_t \boldsymbol{v}_t). \end{aligned}$$

This leads to the following error estimation for the conditional divergence loss:

$$\begin{aligned}&\mathcal{L}_{\mathrm{CDM}}(\theta)\\ :=&\mathbb{E}_{t,p_t(\boldsymbol{x}|\boldsymbol{x}_1),p(\boldsymbol{x}_1)}\Big[\Big|\Big(\nabla\cdot\boldsymbol{u}_t(\boldsymbol{x}|\boldsymbol{x}_1)-\nabla\cdot\boldsymbol{v}_t(\boldsymbol{x},\theta)\Big)\\ &+\Big(\boldsymbol{u}_t(\boldsymbol{x}|\boldsymbol{x}_1)-\boldsymbol{v}_t(\boldsymbol{x},\theta)\Big)\cdot\nabla\log p_t(\boldsymbol{x}|\boldsymbol{x}_1)\Big|\Big].\end{aligned} \tag{14}$$

Now we are ready to establish the fact that the conditional divergence loss $\mathcal{L}_{\mathrm{CDM}}(\theta)$ is an upper bound for the divergence loss $\mathcal{L}_{\mathrm{DM}}(\theta)$ and the TV gap $\mathrm{TV}(p_t,\hat{p}_t)$. We summary our results in the following theorem:

Theorem 4.1. *We have the following inequality:*

$$\mathcal{L}_{\mathrm{DM}}(\theta)\le\mathcal{L}_{\mathrm{CDM}}(\theta). \tag{15}$$

Furthermore, we have:

$$\mathrm{TV}(p_t,\hat{p}_t)\le\frac{1}{2}\mathcal{L}_{\mathrm{CDM}}(\theta), \tag{16}$$

for any $t\in[0,1]$.

4.1. Flow and Divergence Matching.

In practice, we observe that directly minimizing $\mathcal{L}_{\mathrm{CDM}}(\theta)$ cannot yield appealing results as the loss cannot go to exact zero in training. This nonzero loss comes from a balance between $\nabla\cdot\boldsymbol{u}_t(\boldsymbol{x}|\boldsymbol{x}_1)-\nabla\cdot\boldsymbol{v}_t(\boldsymbol{x},\theta)$ and $(\boldsymbol{u}_t(\boldsymbol{x}|\boldsymbol{x}_1)-\boldsymbol{v}_t(\boldsymbol{x},\theta))\cdot\nabla\log p_t(\boldsymbol{x}|\boldsymbol{x}_1)$, and both terms can be positive or negative, resulting in cancellation. As such, there is no guarantee that we can learn a vector field $\boldsymbol{v}_t(\boldsymbol{x},\theta)$ that is in proximity to $\boldsymbol{u}_t(\boldsymbol{x})$ by minimizing $\mathcal{L}_{\mathrm{CDM}}(\theta)$. In contrast, by combining $\mathcal{L}_{\mathrm{CDM}}$ and $\mathcal{L}_{\mathrm{CFM}}$ through a weighted sum in the training objective, we can directly control the gap between the vector fields and their divergences. Therefore, we propose the flow and divergence matching (FDM) loss:

$$\mathcal{L}_{\mathrm{FDM}}=\lambda_1\mathcal{L}_{\mathrm{CFM}}+\lambda_2\mathcal{L}_{\mathrm{CDM}}, \tag{17}$$

where $\lambda_1,\lambda_2>0$ are hyperparameters; we choose them via hyperparameter search in this work. It is an interesting future direction to design a principle to choose λs optimally.

Remark 4.2. It is worth noting that minimizing the objective function $\mathcal{L}_{\mathrm{FDM}}$ offers a more computationally efficient approach compared to high-order control methods presented in (Meng et al., 2021; Lu et al., 2022), as it is computationally much cheaper than controlling differences in high-order quantities, such as the Jacobian or the gradient of the divergence. While a bounded TV distance does not necessarily imply a bound on the KL divergence, we leave the exploration of developing a computationally efficient method for controlling the KL divergence in this direction for future work.

4.2. Synthetic Experiment.

To solidify our theoretical results, we present a simple numerical example before moving to real-world applications. Specifically, we consider the problem of sampling from the following Gaussian mixture distribution

$$\begin{aligned}p(\boldsymbol{x})=&0.23\mathcal{N}(-3,0.1)+0.35\mathcal{N}(-1,0.1)\\ &+0.15\mathcal{N}(-1,0.1)+0.27\mathcal{N}(3,0.1),\end{aligned} \tag{18}$$

using both standard FM and our proposed FDM defined in equation (17). We use a 3-layer MLP to approximate the VP diffusion path vector field by minimizing equation (17) with $\lambda_1=1,\lambda_2=0$ for FM and $\lambda_1=1,\lambda_2=0.2$ for FDM. We use 10^4 data points sampled from equation (18) for training.

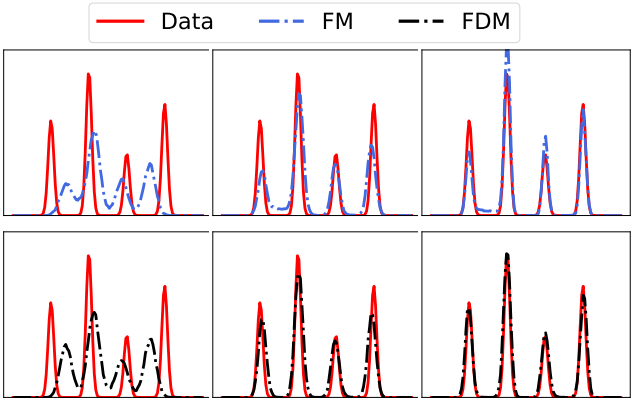

Figure 2. Snapshots for probability paths at $t=0.6,0.85$, and 1 (left to right). First/Second row: FM/FDM vs. data distribution.

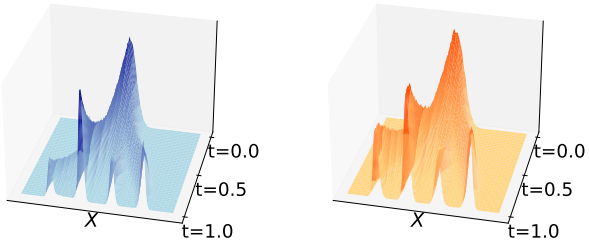

Figure 3. Comparison of probability paths over time learned by FM (left) vs. FDM (right).

Figures 2 and 3 contrast the performance of our proposed FDM against the benchmark FM. The numerical results confirm that the probability path (at $t=1$) learned by FM suffers from a substantial discrepancy from the exact Gaussian mixture distribution. In contrast, FDM learns the Gaussian mixture much more accurately than FM. Specifically, the TV gaps between the learned and exact distributions are 0.0945 and 0.0587 for FM and FDM, respectively.

5. Experimental Results

In this section, we validate the efficacy and efficiency of the proposed FDM in enhancing FM across various benchmark tasks, including density estimation on synthetic 2D data (Section 5.1.1) and image data (Section 5.1.2), DNA sequence generation (Section 5.2), and spatiotemporal data sampling tasks including trajectory sampling for dynamical systems (Section 5.3.1) and video prediction via latent FM (Section 5.3.2).

Our experiments confirm that our proposed FDM remarkably improves FM with guidance, enhancing promoter DNA sequence design with class-conditional flow, as well as refining trajectory generation for dynamical systems and video predictions conditioning on the initial states over the first several time steps. In this section, we report the error between the exact and learned distributions in terms of the TV distance, and the corresponding KL divergence results are further provided in Appendix C.

Software and Equipment. Our implementation utilizes PyTorch Lightning (Falcon, 2019) for synthetic density estimation, DNA sequence generation, and video generation, while JAX (Bradbury et al., 2018) and TensorFlow (Abadi et al., 2016) are employed for dynamical systems-related experiments. Experiments are conducted on multiple NVIDIA RTX 3090 GPUs.

Training Setup. See Appendix B.

Models and Datasets. We employ OT and VE/VP diffusion paths for the flow maps in most tasks except the Dirichlet flow for DNA generation. We follow the approach used in (Huang et al., 2024; Lu et al., 2022) to estimate the divergence, which employs Hutchinson's trace estimator (Hutchinson, 1989). Our experiments utilize a numerical simulation-based dataset for density estimation and trajectory sampling, a dataset extracted from a database of human promoters (Hon et al., 2017) for DNA design, and the KTH human motion dataset (Schuldt et al., 2004) and the BAIR Robot Pushing dataset (Ebert et al., 2017) for video prediction.

Model	FM (OT)	FDM (OT)	FM (VP)	FDM (VP)
Likelihood (↑)	$2.38_{\pm.02}$	$\mathbf{2.53}_{\pm.02}$	$2.34_{\pm.02}$	$2.46_{\pm.02}$

Table 1. Likelihood estimation of models on the checkerboard test set. Here, "OT" denotes the optimal transport path and "VP" denotes the variance-preserving path. Unit: $\times 10^{-2}$

5.1. Density Estimation on Synthetic and Image Data

We train the models for density estimation on two datasets: a synthetic 2D checkerboard and the image dataset CIFAR-10 (Krizhevsky et al., 2009).

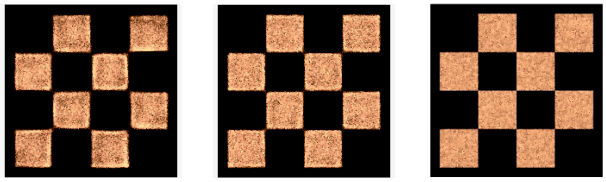

(a) FM (OT) (b) FDM (OT) (c) Ground Truth

Figure 4. Generated samples from FM and FDM using the optimal transport (OT) path trained on the checkerboard dataset.

5.1.1. Synthetic density estimation

In this experiment, we train models using FM and FDM for 2×10^4 iterations using a batch size of 512. For each iteration, we numerically sample the data for the training set and use the same sampling method for validation and testing sets. We compare FM and FDM with the baselines for both OT and VP paths in the likelihood computed based on the test dataset. The results in Table 1 and Fig. 4 show that FDM consistently outperforms FM across different probability paths.

5.1.2. Density Modeling on Image Datasets

In the experiment, we we train models using both FM and FDM for image sampling on CIFAR10 dataset (Krizhevsky et al., 2009), we follow the experimental settings in the flow matching baseline paper (Lipman et al., 2023) and compare the performance in terms of the negative log-likelihood and FID scores of the sampled images as shown in Table 2.

Model	NLL(↓)	FID(↓)
FM(OT)	2.99	6.35
FDM(OT)	2.85	5.62

Table 2. Negative log-likelihood and sample quality (FID scores) estimation on CIFAR-10.

5.2. Sequential Data Sampling–DNA Sequence

In this experiment, we demonstrate that FDM enhances FM with the conditional OT path and Dirichlet path (Stark et al., 2024) on the probability simplex for DNA sequence generation, both with and without guidance, following experiments conducted in (Stark et al., 2024). For this task, instead of directly parameterizing the vector field, the Dirichlet flow model constructs it by combining pre-designed Dirichlet probability path functions with a parameterized classifier $\hat{p}_t(\boldsymbol{x}_1|\boldsymbol{x}, \theta)$, where $\boldsymbol{x}$ is sampled from the conditional probability at time t, given the data point $\boldsymbol{x}_1$. Since $\boldsymbol{x}_1$ represents discrete categorical data with a finite number of categories, it can be treated as a class label. Since this approach only requires parameterizing the classifier $\hat{p}_t(\boldsymbol{x}_1|\boldsymbol{x}, \theta)$, we only need to penalize the norm of the gradient with respect to

the input of the classifier, which is equivalent to minimizing the divergence error; see Appendix B.2 for more details. Additionally, we conduct experiments where the classifier is parameterized with guidance, $p_t(\boldsymbol{x}_1|\boldsymbol{x}, \boldsymbol{y}, \theta)$ with $\boldsymbol{y}$ representing the guiding information. We use the same experiment setup in (Stark et al., 2024) except the newly introduced hyperparameters λ_1 and λ_2; see Appendix B.2 for the detailed settings.

5.2.1. Simplex Dimension without Guidance

We first evaluate the performance of FM and FDM in a non-guided simple generation task. The data is sampled from a uniform Dirichlet distribution with a sequence length of $l = 4$ and $K = 40$ categories. We compare the TV distance and KL divergence between the generated distribution and the target distribution on the test dataset. The results in Table 14 in Appendix C.1 demonstrate that FDM outperforms FM in generating the simple sequential categorical data.

Method	TV Distance	Time (s/iter)
Linear FM	$0.12_{\pm 0.005}$	0.10
Linear FDM	$0.10_{\pm 0.004}$	0.16
Dirichlet FM	$0.08_{\pm 0.005}$	0.10
Dirichlet FDM	$\mathbf{0.07}_{\pm 0.004}$	0.16

Table 3. TV distances between the generated and target distributions.

5.2.2. Promoter DNA Sequence Design with Guidance

We further evaluate the ability of FM and FDM in training generative models for designing DNA promoter sequences guided by a desired promoter profile. We train the models guided by a profile by providing it as additional input to the vector field and evaluate generated sequences using mean-squared error (MSE) between their predicted and original regulatory activity, as determined by SEI (Chen et al., 2022). We include the discrete DM (Albergo et al., 2023) and the language model (Stark et al., 2024) for comparison in Table 4. For this task, we use a dataset of 100,000 promoter sequences with 1024 base pairs extracted from a database of human promoters (Hon et al., 2017). See Appendix B.2 for more details about the dataset. The results confirm that FDM improves FM in training guided models for categorical data generation.

Method	MSE (↓)
Bit Diffusion (One-hot Encoding)(Albergo et al., 2023)	3.95E-2
DDSM (Albergo et al., 2023)	3.34E-2
Large Language Model (Stark et al., 2024)	3.33E-2
Linear FM (Stark et al., 2024)	$2.82_{\pm 0.02}$E-2
Linear FDM (ours)	$2.78_{\pm 0.01}$E-2
Dirichlet FM (Stark et al., 2024)	$2.68_{\pm 0.01}$E-2
Dirichlet FDM (ours)	$\mathbf{2.59}_{\pm 0.02}$E-2

Table 4. Evaluation of transcription profile guided promoter DNA sequence design of different models.

5.3. Spatiotemperal Data Generation

In this section, we evaluate our model on spatiotemporal data sampling tasks, both with and without guidance. Specifically, we consider two scenarios: trajectory sampling for dynamical systems and video generation.

5.3.1. Trajectory Sampling for Dynamical Systems

Sampling trajectories for dynamical systems under event guidance is crucial for understanding and predicting the climate and beyond (Perkins & Alexander, 2013; Mosavi et al., 2018; Hochman et al., 2019). Finzi et al. (2023) develop a DM for sampling these events.

In this experiment, we compare FDM against FM and DM from (Finzi et al., 2023) on the Lorenz and FitzHugh-Nagumo models (Farazmand & Sapsis, 2019); the details of these models are provided in Appendix B.1. We test sampling trajectories from these systems with and without event guidance. A trajectory, either from a dataset or sampled, is a discrete time series of vectors concatenated into $\boldsymbol{x}_1 = [\boldsymbol{x}(\tau_m)]_{m=1}^M \in \mathbb{R}^{Md}$, where M is the number of time steps and d is the dimension of the system. Following (Finzi et al., 2023), an event E is a set of trajectories characterized by some event constraint; for example, $E = \{\boldsymbol{x}_1 : C(\boldsymbol{x}_1) > 0\}$, where the event constraint function $C : \mathbb{R}^{Md} \to \mathbb{R}$ is smooth. The challenge of this experiment is to sample trajectories in E when C is only known after the models been trained. The detailed sampling procedure using DM can be found in (Finzi et al., 2023).

The event-guided sampling procedure from (Finzi et al., 2023) uses Tweedie's formula (Robbins, 1992; Efron, 2011), which requires the score function $\nabla \log p_t(\boldsymbol{x})$. Since FM and FDM are not trained to approximate $\nabla \log p_t(\boldsymbol{x})$ directly, we derive an approximation formula using the learned vector field $\boldsymbol{v}_t(\boldsymbol{x}, \theta)$. Applying Lemma 1 of (Lipman et al., 2023) to the probability flow ODE (Song et al., 2020), the evolution of $p_t(\boldsymbol{x})$ satisfies:

$$\boldsymbol{u}_t(\boldsymbol{x}) = -\boldsymbol{f}(\boldsymbol{x}, 1-t) + \frac{1}{2} g^2(1-t) \nabla \log p_{1-t}(\boldsymbol{x}), \quad (19)$$

where $\boldsymbol{f}$ is the drift term and g is the noise coefficient. Rearranging equation (19), we express $\nabla \log p_t(\boldsymbol{x})$ in terms of $\boldsymbol{u}_t(\boldsymbol{x})$, then approximate $\boldsymbol{u}_t(\boldsymbol{x})$ by $\boldsymbol{v}_t(\boldsymbol{x}, \theta)$.

We use the events defined in (Finzi et al., 2023) for our experiments. The event for the Lorenz system is when a trajectory stays on one arm of the chaotic attractor. This is characterized by $C(\boldsymbol{x}) = 0.6 - \|F[\boldsymbol{x} - \overline{\boldsymbol{x}}]\|_1 > 0$, where F is the Fourier transform over trajectory time τ, $\|\cdot\|_1$ is the

1-norm summing over both over the frequency magnitudes and the three dimensions of $\boldsymbol{x}(\tau)$, and $\overline{\boldsymbol{x}}$ is the average of $\boldsymbol{x}(\tau)$ over τ. For the FitzHugh-Nagumo system, the event is neuron spiking, which is characterized by $C(\boldsymbol{x}) = \max_\tau [x_1(\tau) + x_2(\tau)]/2 - 2.5 > 0$.

We compare the models' ability to generate trajectories according to $p(\boldsymbol{x}_1)$ and $p(\boldsymbol{x}_1|E)$ by computing a test set of trajectories using the Dormand-Prince ODE solver (Dormand & Prince, 1980) and sampling trajectories using each model. Table 5 presents the TV distance between the model and the distributions. From the result, we observe that FDM achieves the lowest TV distance for every distribution. The TV distance of FDM is smaller than that of FM, which empirically demonstrates that the divergence mismatch has a significant effect on the error $\epsilon_t(\boldsymbol{x}_t)$.

Furthermore, this shows that the proposed loss $\mathcal{L}_{\text{FDM}}$ effectively reduces the mismatch. This mismatch reduction also enables FDM to attain the lowest negative log-likelihood (NLL) estimates. Table 6 shows the mean NLL over trajectories and trajectory dimension with respect to to $p(\boldsymbol{x}_1)$, while Fig. 5 compares the histograms of the event constraint value of each event trajectory. Importantly, these improvements of FDM do not trade off with its accuracy in estimating $p(E)$. When $p(E)$ is estimated based on the proportion of sampled trajectories that fall within E, all the models are comparable. Table 7 reports the KL divergence between the histograms of the event constraint value $C(\boldsymbol{x}_1)$ for event trajectories $\boldsymbol{x}_1$ from the dataset computed by an ODE solver and those sampled with event guidance from the models. The results show that our FDM consistently outperforms both the FM and Diffusion models.

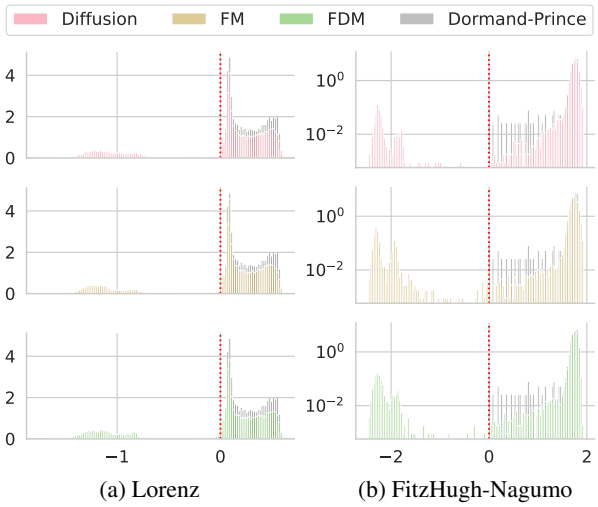

(a) Lorenz (b) FitzHugh-Nagumo

Figure 5. Histograms of the constraint value $C(\boldsymbol{x}_1)$ where $\boldsymbol{x}_1$ is an event trajectory computed by the Dormand-Prince ODE solver or sampled from the model with event guidance. The unguided sampling histograms are shown in Appendix C.2.

Model	Lorenz		FitzHugh-Nagumo	
	$p(\boldsymbol{x}_1)$ (↓)	$p(\boldsymbol{x}_1\|E)$ (↓)	$p(\boldsymbol{x}_1)$ (↓)	$p(\boldsymbol{x}_1\|E)$ (↓)
Diffusion	0.0314	0.1001	0.0277	0.1192
FM	0.0348	0.0972	0.0314	0.2164
FDM(ours)	**0.0306**	**0.0914**	**0.0266**	**0.1168**

Table 5. TV distances of the models from the trajectory distribution $p(\boldsymbol{x}_1)$ and from the distribution conditioned on an event $p(\boldsymbol{x}_1|E)$. Here, Diffusion results follow from (Finzi et al., 2023), while FM and FDM are based on our implementation, which builds on the code provided by Finzi et al. (2023).

Model	Lorenz		FitzHugh-Nagumo	
	NLL($\boldsymbol{x}_1$) (↓)	$p(E)$	NLL($\boldsymbol{x}_1$) (↓)	$p(E)$
Dormand-Prince	–	0.197	–	0.035
Diffusion	-7.052	0.200	-7.365	0.032
FM	-13.190	0.199	-13.942	0.034
FDM	**-14.361**	0.200	**-14.408**	0.033

Table 6. NLLs averaged over trajectories and trajectory dimension with respect to the trajectory distribution $p(\boldsymbol{x}_1)$, and the likelihood of the user-defined event estimated by the proportion of trajectories contained in event E sampled from the model without guidance. Here, the Diffusion follows from (Finzi et al., 2023). FM and FDM are based on our own implementation.

Model	Lorenz		FitzHugh-Nagumo	
	$p(\boldsymbol{x}_1)$	$p(\boldsymbol{x}_1\|E)$	$p(\boldsymbol{x}_1)$	$p(\boldsymbol{x}_1\|E)$
Diffusion	0.0056	0.2774	0.0260	0.3011
FM	0.0081	**0.2560**	0.0280	0.3468
FDM(ours)	**0.0049**	0.3045	**0.0280**	**0.2084**

Table 7. KL divergence between the histograms of the event constraint value $C(\boldsymbol{x}_1)$ for event trajectories $\boldsymbol{x}_1$ in the dataset of trajectories computed by an ODE solver and event trajectories sampled with event guidance from the models.

5.3.2. Generative Modeling for Videos

We aim to show how FDM pushes the boundary of FM performance for sequential data generation in a latent space. We train a latent FM (Davtyan et al., 2023) and a latent FDM for video prediction. We further utilize a pre-trained VQGAN (Esser et al., 2021) to encode (resp. decode) each frame of the video to (resp. from) the latent space. We train the models guided by the latent state at $t-1$ and $t-\tau$, where τ is randomly selected from $\{2, .., t\}$, via providing them as additional input guidance to the vector field at $t > C$, where C is a positive integer. At inference time, we use the frames at time $t = 0$ to $t = C$ of a video as the guidance and then utilize flow matching to predict the frames after $t = C$.

We consider the human motion dataset – KTH (Schuldt et al., 2004) and BAIR Robot Pushing dataset (Ebert et al., 2017). We follow the experimental setup of (Davtyan et al., 2023); see Appendix B.3 for details. To evaluate the generated samples, we compute the Frechet video distance (FVD) (Unterthiner et al., 2018) and peak signal-to-noise ratio (PSNR) (Huynh-Thu & Ghanbari, 2008).

KTH Dataset: For KTH, we use the first 10 frames as

guidance and predict the next 30 frames. The results in Table 8 indicate that FDM enhances latent FM for temporal data generation. Furthermore, Fig. 6 presents illustrative cases showing that our FDM consistently maintains high visual quality throughout the video, whereas the FM model exhibits noticeable degradation in later frames, including loss of fine motion details, missing body parts, and motion failure.

BAIR Dataset: For BAIR, we predict 15 future frames based on a single initial frame, with each frame having a resolution of 64×64 pixels. Because of the highly stochastic motion in the BAIR dataset, following (Davtyan et al., 2023), we generate 100 samples per test video – each conditioned on the same initial frame – and compute metrics over 100×256 generated samples against 256 randomly selected test videos. To highlight the effectiveness of FDM, we omit the frame refinement step used in (Davtyan et al., 2023). As mentioned in (Davtyan et al., 2023), many models for the BAIR task are computationally expensive, whereas latent FM achieves a favorable trade-off between FVD and computational cost. Our approach further improves latent FM with acceptable additional computational overhead, as shown in Table 9.

We notice that the experiments in Chen et al. (2024) achieve very impressive results for video generation, and it is an interesting future direction to integrate our approach into their framework.

Method	FVD(↓)	PSNR(↑)	Time(s/iter)
SRVP (Franceschi et al., 2020)	222	29.7	–
SLAMP (Akan et al., 2021)	228	29.4	–
Latent FM (Davtyan et al., 2023)	180	30.4	0.18
Latent FDM (ours)	**155.5**$_{\pm 5}$	**31.2**	0.27

Table 8. KTH dataset evaluation. The evaluation protocol is to predict the next 30 frames given the first 10 frames.

Method	FVD(↓)	MEM(GB)	Time(hours)
TriVD-GAN-FP (Luc et al., 2020)	103	1024	280
Video Transformer (Weissenborn et al., 2019)	94	512	336
LVT (Rakhimov et al., 2020)	126	128	48
RaMViD (Diffusion) (Höppe et al., 2022)	84	320	72
Latent FM (Davtyan et al., 2023)	146	24.2	25
Latent FDM (ours)	**123**$_{\pm 4.5}$	35	36

Table 9. BAIR dataset evaluation. We adopt the standard evaluation setup, where the model predicts 15 future frames conditioned on a single initial frame. MEM stands for peak memory footprint.

6. Concluding Remarks

In this paper, we have developed a new upper bound for the gap between learned and ground-truth probability paths using FM. Our new error bound shows that FM can be improved by ensuring the divergences of the vector fields are in proximity. To achieve this, we derive a new conditional divergence loss with computational efficiency. Our new training approach – flow and divergence matching – significantly improves FM on various challenging tasks. There are several avenues for future work. A particularly intriguing direction is to develop a computationally efficient method for controlling the KL divergence, for example by integrating deep equilibrium models (Bai et al., 2019) into our framework – similar to how prior works have incorporated them into diffusion (score-based) models (Huang et al., 2024; Bai & Melas-Kyriazi, 2024). This remains an open problem and an important avenue for future research. Moreover, exploring our approach in the Schrödinger bridge setting (Tong et al., 2024) is also an interesting problem.

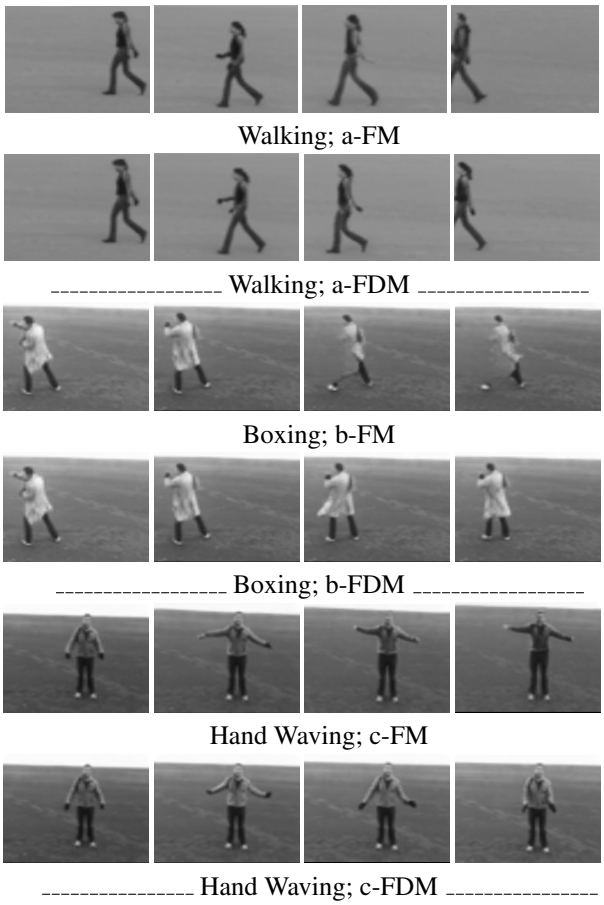

Figure 6. Samples on KTH human motion dataset – at frame 0, 13, 27, 40 from left to right – generated by latent FM (a-FM, b-FM, c-FM) and latent FDM (a-FDM, b-FDM, c-FDM). These cases show the exhibits noticeable degradation in later frames, including loss of fine motion details, missing body parts, and motion failure.

Acknowledgement

This material is based on research sponsored by NSF grants DMS-2152762, DMS-2208361, DMS-2219956, and DMS-2436344, and DOE grants DE-SC0023490, DE-SC0025589, and DE-SC0025801. HZ acknowledges the support from the U.S. Department of Energy, Office of Science, Office of Advanced Scientific Computing Research research grant DOE-FOA-2493 "Data-intensive scientific machine learning", under contract DE-AC02-06CH11357 at Argonne National Laboratory.

Impact Statement

This work presents a new theoretical bound on the gap between the exact and learned probability paths using flow matching. The new theoretical bound informs the design of a new efficient training objective to improve flow matching. Our work directly contributes to advancing flow-based generative modeling. Flow-based models have achieved remarkable results in climate modeling and molecular modeling. By developing new theoretical understandings and fundamental algorithms with performance guarantees, we expect our work will advance climate modeling and molecular sciences using generative models. Our work contributes to basic research, and we do not see potential ethical concerns or negative societal impact beyond the current AI.

References

Abadi, M., Barham, P., Chen, J., Chen, Z., Davis, A., Dean, J., Devin, M., Ghemawat, S., Irving, G., Isard, M., et al. {TensorFlow}: a system for {Large-Scale} machine learning. In *12th USENIX symposium on operating systems design and implementation (OSDI 16)*, pp. 265–283, 2016.

Akan, A. K., Erdem, E., Erdem, A., and Güney, F. Slamp: Stochastic latent appearance and motion prediction. In *Proceedings of the IEEE/CVF International Conference on Computer Vision*, pp. 14728–14737, 2021.

Akiba, T., Sano, S., Yanase, T., Ohta, T., and Koyama, M. Optuna: A next-generation hyperparameter optimization framework. In *Proceedings of the 25th ACM SIGKDD International Conference on Knowledge Discovery and Data Mining*, 2019.

Albergo, M. S. and Vanden-Eijnden, E. Building normalizing flows with stochastic interpolants. In *The Eleventh International Conference on Learning Representations*, 2023. URL https://openreview.net/forum?id=li7qeBbCR1t.

Albergo, M. S., Boffi, N. M., and Vanden-Eijnden, E. Stochastic interpolants: A unifying framework for flows and diffusions. *arXiv preprint arXiv:2303.08797*, 2023.

Bai, S., Kolter, J. Z., and Koltun, V. Deep equilibrium models. *Advances in neural information processing systems*, 32, 2019.

Bai, X. and Melas-Kyriazi, L. Fixed point diffusion models. In *Proceedings of the IEEE/CVF Conference on Computer Vision and Pattern Recognition*, pp. 9430–9440, 2024.

Bao, F., Nie, S., Xue, K., Cao, Y., Li, C., Su, H., and Zhu, J. All are worth words: A vit backbone for diffusion models. In *Proceedings of the IEEE/CVF conference on computer vision and pattern recognition*, pp. 22669–22679, 2023.

Bose, J., Akhound-Sadegh, T., Huguet, G., FATRAS, K., Rector-Brooks, J., Liu, C.-H., Nica, A. C., Korablyov, M., Bronstein, M. M., and Tong, A. SE(3)-stochastic flow matching for protein backbone generation. In *The Twelfth International Conference on Learning Representations*, 2024. URL https://openreview.net/forum?id=kJFIH23hXb.

Bradbury, J., Frostig, R., Hawkins, P., Johnson, M. J., Leary, C., Moritz, P., Paszke, A., VanderPlas, J., Wanderman-Milne, S., and Zhang, Q. Jax: Autograd and xla. *GitHub repository*, 2018.

Chen, K. M., Wong, A. K., Troyanskaya, O. G., and Zhou, J. A sequence-based global map of regulatory activity for deciphering human genetics. *Nature genetics*, 54(7): 940–949, 2022.

Chen, R. T., Rubanova, Y., Bettencourt, J., and Duvenaud, D. K. Neural ordinary differential equations. *Advances in neural information processing systems*, 31, 2018.

Chen, R. T. Q. and Lipman, Y. Flow matching on general geometries. In *The Twelfth International Conference on Learning Representations*, 2024. URL https://openreview.net/forum?id=g7ohDlTITL.

Chen, Y., Goldstein, M., Hua, M., Albergo, M. S., Boffi, N. M., and Vanden-Eijnden, E. Probabilistic forecasting with stochastic interpolants and föllmer processes. In Salakhutdinov, R., Kolter, Z., Heller, K., Weller, A., Oliver, N., Scarlett, J., and Berkenkamp, F. (eds.), *Proceedings of the 41st International Conference on Machine Learning*, volume 235 of *Proceedings of Machine Learning Research*, pp. 6728–6756. PMLR, 21–27 Jul 2024. URL https://proceedings.mlr.press/v235/chen24n.html.

Davtyan, A., Sameni, S., and Favaro, P. Efficient video prediction via sparsely conditioned flow matching. In *Proceedings of the IEEE/CVF International Conference on Computer Vision*, pp. 23263–23274, 2023.

Delecki, H., Schlichting, M. R., Arief, M., Corso, A., Vazquez-Chanlatte, M., and Kochenderfer, M. J. Diffusion-based failure sampling for cyber-physical systems. *arXiv preprint arXiv:2406.14761*, 2024.

Dormand, J. R. and Prince, P. J. A family of embedded runge-kutta formulae. *Journal of computational and applied mathematics*, 6(1):19–26, 1980.

Ebert, F., Finn, C., Lee, A. X., and Levine, S. Self-supervised visual planning with temporal skip connections. *CoRL*, 12(16):23, 2017.

Efron, B. Tweedie's formula and selection bias. *Journal of the American Statistical Association*, 106(496):1602–1614, 2011.

Esser, P., Rombach, R., and Ommer, B. Taming transformers for high-resolution image synthesis. In *Proceedings of the IEEE/CVF conference on computer vision and pattern recognition*, pp. 12873–12883, 2021.

Falcon, W. Pytorch lightning. *GitHub. Note: https://github.com/Lightning-AI/lightning*, 2019.

Farazmand, M. and Sapsis, T. P. Extreme events: Mechanisms and prediction. *Applied Mechanics Reviews*, 71(5): 050801, 2019.

Finzi, M. A., Boral, A., Wilson, A. G., Sha, F., and Zepeda-Núñez, L. User-defined event sampling and uncertainty quantification in diffusion models for physical dynamical systems. In *International Conference on Machine Learning*, pp. 10136–10152. PMLR, 2023.

FitzHugh, R. Impulses and physiological states in theoretical models of nerve membrane. *Biophysical journal*, 1 (6):445–466, 1961.

Franceschi, J.-Y., Delasalles, E., Chen, M., Lamprier, S., and Gallinari, P. Stochastic latent residual video prediction. In *International Conference on Machine Learning*, pp. 3233–3246. PMLR, 2020.

Frans, K., Hafner, D., Levine, S., and Abbeel, P. One step diffusion via shortcut models. *arXiv preprint arXiv:2410.12557*, 2024.

Grathwohl, W., Chen, R. T., Bettencourt, J., Sutskever, I., and Duvenaud, D. Ffjord: Free-form continuous dynamics for scalable reversible generative models. *arXiv preprint arXiv:1810.01367*, 2018.

Hochman, A., Alpert, P., Harpaz, T., Saaroni, H., and Messori, G. A new dynamical systems perspective on atmospheric predictability: Eastern mediterranean weather regimes as a case study. *Science advances*, 5(6):eaau0936, 2019.

Hon, C.-C., Ramilowski, J. A., Harshbarger, J., Bertin, N., Rackham, O. J., Gough, J., Denisenko, E., Schmeier, S., Poulsen, T. M., Severin, J., et al. An atlas of human long non-coding rnas with accurate 5' ends. *Nature*, 543 (7644):199–204, 2017.

Höppe, T., Mehrjou, A., Bauer, S., Nielsen, D., and Dittadi, A. Diffusion models for video prediction and infilling. *arXiv preprint arXiv:2206.07696*, 2022.

Hua, X., Ahmad, R., Blanchet, J., and Cai, W. Accelerated sampling of rare events using a neural network bias potential. *arXiv preprint arXiv:2401.06936*, 2024.

Huang, Y., Wang, Q., Onwunta, A., and Wang, B. Efficient score matching with deep equilibrium layers. In *The Twelfth International Conference on Learning Representations*, 2024. URL https://openreview.net/forum?id=J1djqLAa6N.

Hutchinson, M. F. A stochastic estimator of the trace of the influence matrix for laplacian smoothing splines. *Communications in Statistics-Simulation and Computation*, 18(3):1059–1076, 1989.

Huynh-Thu, Q. and Ghanbari, M. Scope of validity of psnr in image/video quality assessment. *Electronics letters*, 44 (13):800–801, 2008.

Jing, B., Berger, B., and Jaakkola, T. Alphafold meets flow matching for generating protein ensembles. In *NeurIPS 2023 Generative AI and Biology (GenBio) Workshop*, 2023. URL https://openreview.net/forum?id=yQcebEgQfH.

Krizhevsky, A., Hinton, G., et al. Learning multiple layers of features from tiny images. 2009.

Lai, C.-H., Takida, Y., Murata, N., Uesaka, T., Mitsufuji, Y., and Ermon, S. Fp-diffusion: Improving score-based diffusion models by enforcing the underlying score fokker-planck equation. In *International Conference on Machine Learning*, pp. 18365–18398. PMLR, 2023.

Li, L., Carver, R., Lopez-Gomez, I., Sha, F., and Anderson, J. Generative emulation of weather forecast ensembles with diffusion models. *Science Advances*, 10(13):eadk4489, 2024.

Lipman, Y., Chen, R. T. Q., Ben-Hamu, H., Nickel, M., and Le, M. Flow matching for generative modeling. In *The Eleventh International Conference on Learning Representations*, 2023. URL https://openreview.net/forum?id=PqvMRDCJT9t.

Liu, X., Gong, C., and Liu, Q. Flow straight and fast: Learning to generate and transfer data with rectified flow. In *The Eleventh International Conference on Learning*

Representations, 2023. URL https://openreview.net/forum?id=XVjTT1nw5z.

Lorenz, E. N. Deterministic nonperiodic flow. *Journal of atmospheric sciences*, 20(2):130–141, 1963.

Lu, C., Zheng, K., Bao, F., Chen, J., Li, C., and Zhu, J. Maximum likelihood training for score-based diffusion odes by high order denoising score matching. In *International Conference on Machine Learning*, pp. 14429–14460. PMLR, 2022.

Luc, P., Clark, A., Dieleman, S., Casas, D. d. L., Doron, Y., Cassirer, A., and Simonyan, K. Transformation-based adversarial video prediction on large-scale data. *arXiv preprint arXiv:2003.04035*, 2020.

Meng, C., Song, Y., Li, W., and Ermon, S. Estimating high order gradients of the data distribution by denoising. *Advances in Neural Information Processing Systems*, 34: 25359–25369, 2021.

Mosavi, A., Ozturk, P., and Chau, K.-w. Flood prediction using machine learning models: Literature review. *Water*, 10(11):1536, 2018.

Nagumo, J., Arimoto, S., and Yoshizawa, S. An active pulse transmission line simulating nerve axon. *Proceedings of the IRE*, 50(10):2061–2070, 1962.

Perkins, S. E. and Alexander, L. V. On the measurement of heat waves. *Journal of climate*, 26(13):4500–4517, 2013.

Petersen, M., Roig, G., and Covino, R. Dynamicsdiffusion: Generating and rare event sampling of molecular dynamic trajectories using diffusion models. In *NeurIPS 2023 AI for Science Workshop*.

Rakhimov, R., Volkhonskiy, D., Artemov, A., Zorin, D., and Burnaev, E. Latent video transformer. *arXiv preprint arXiv:2006.10704*, 2020.

Robbins, H. E. An empirical bayes approach to statistics. In *Breakthroughs in Statistics: Foundations and basic theory*, pp. 388–394. Springer, 1992.

Schuldt, C., Laptev, I., and Caputo, B. Recognizing human actions: a local svm approach. In *Proceedings of the 17th International Conference on Pattern Recognition, 2004. ICPR 2004.*, volume 3, pp. 32–36. IEEE, 2004.

Seis, C. A quantitative theory for the continuity equation. In *Annales de l'Institut Henri Poincaré C, Analyse non linéaire*, volume 34, pp. 1837–1850. Elsevier, 2017.

Shiraki, T., Kondo, S., Katayama, S., Waki, K., Kasukawa, T., Kawaji, H., Kodzius, R., Watahiki, A., Nakamura, M., Arakawa, T., et al. Cap analysis gene expression for high-throughput analysis of transcriptional starting point and identification of promoter usage. *Proceedings of the National Academy of Sciences*, 100(26):15776–15781, 2003.

Song, Y. and Dhariwal, P. Improved techniques for training consistency models. *arXiv preprint arXiv:2310.14189*, 2023.

Song, Y., Sohl-Dickstein, J., Kingma, D. P., Kumar, A., Ermon, S., and Poole, B. Score-based generative modeling through stochastic differential equations. *arXiv preprint arXiv:2011.13456*, 2020.

Song, Y., Durkan, C., Murray, I., and Ermon, S. Maximum likelihood training of score-based diffusion models. *Advances in neural information processing systems*, 34: 1415–1428, 2021.

Stark, H., Jing, B., Wang, C., Corso, G., Berger, B., Barzilay, R., and Jaakkola, T. Dirichlet flow matching with applications to dna sequence design. *arXiv preprint arXiv:2402.05841*, 2024.

Tong, A. Y., Malkin, N., Fatras, K., Atanackovic, L., Zhang, Y., Huguet, G., Wolf, G., and Bengio, Y. Simulation-free schrödinger bridges via score and flow matching. In *International Conference on Artificial Intelligence and Statistics*, pp. 1279–1287. PMLR, 2024.

Unterthiner, T., Van Steenkiste, S., Kurach, K., Marinier, R., Michalski, M., and Gelly, S. Towards accurate generative models of video: A new metric & challenges. *arXiv preprint arXiv:1812.01717*, 2018.

Villani, C. et al. *Optimal transport: old and new*, volume 338. Springer, 2009.

Wan, Z. Y., Baptista, R., Boral, A., Chen, Y.-F., Anderson, J., Sha, F., and Zepeda-Núñez, L. Debias coarsely, sample conditionally: Statistical downscaling through optimal transport and probabilistic diffusion models. *Advances in Neural Information Processing Systems*, 36:47749–47763, 2023.

Weissenborn, D., Täckström, O., and Uszkoreit, J. Scaling autoregressive video models. *arXiv preprint arXiv:1906.02634*, 2019.

Yim, J., Stärk, H., Corso, G., Jing, B., Barzilay, R., and Jaakkola, T. S. Diffusion models in protein structure and docking. *Wiley Interdisciplinary Reviews: Computational Molecular Science*, 14(2):e1711, 2024.

Appendix for
Improving Flow Matching by Aligning Flow Divergence

A. Missing Proofs

Proposition 3.1. *$\epsilon_t \coloneqq p_t - \hat{p}_t$ satisfies the following PDE:*

$$\begin{cases} \partial_t \epsilon_t + \nabla \cdot \big(\epsilon_t \boldsymbol{v}_t\big) = L_t, \\ \epsilon_0(\boldsymbol{x}) = 0, \end{cases} \tag{7}$$

where

$$L_t = -p_t \Big[\nabla \cdot (\boldsymbol{u}_t - \boldsymbol{v}_t) + (\boldsymbol{u}_t - \boldsymbol{v}_t) \cdot \nabla \log p_t\Big]. \tag{8}$$

Proof of Proposition 3.1. For simplicity, we denote $\frac{\partial}{\partial t}$ by ∂_t. From the continuity equations 5 and 6, we have:

$$\begin{aligned} \partial_t \epsilon_t &= \partial_t p_t - \partial_t \hat{p}_t \\ &= \Big[-p_t\big(\nabla \cdot \boldsymbol{u}_t\big) - \boldsymbol{u}_t \cdot \nabla p_t\Big] - \Big[-\hat{p}_t\big(\nabla \cdot \boldsymbol{v}_t\big) - \boldsymbol{v}_t \cdot \nabla \hat{p}_t\Big] \\ &= -p_t\big(\nabla \cdot \boldsymbol{u}_t\big) + \hat{p}_t\big(\nabla \cdot \boldsymbol{v}_t\big) - \boldsymbol{u}_t \cdot \nabla p_t + \boldsymbol{v}_t \cdot \nabla \hat{p}_t \\ &= -p_t\big(\nabla \cdot (\boldsymbol{u}_t - \boldsymbol{v}_t)\big) - (\nabla \cdot \boldsymbol{v}_t)\epsilon_t - (\boldsymbol{u}_t - \boldsymbol{v}_t) \cdot \nabla p_t - \boldsymbol{v}_t \cdot \nabla \epsilon_t \end{aligned} \tag{20}$$

Rewriting it, we find:

$$\partial_t \epsilon_t + \nabla \cdot (\epsilon_t \boldsymbol{v}_t) = -p_t\big(\nabla \cdot (\boldsymbol{u}_t - \boldsymbol{v}_t)\big) - p_t(\boldsymbol{u}_t - \boldsymbol{v}_t) \cdot \nabla \log p_t \tag{21}$$

Let us define $L_t \coloneqq -p_t\big(\nabla \cdot (\boldsymbol{u}_t - \boldsymbol{v}_t)\big) - p_t(\boldsymbol{u}_t - \boldsymbol{v}_t) \cdot \nabla \log p_t$. This gives the following PDE for ϵ_t with the initial condition $\epsilon_0 = p_0 - \hat{p}_0 = 0$:

$$\begin{cases} \partial_t \epsilon_t + \nabla \cdot \Big(\epsilon_t \boldsymbol{v}_t\Big) = L_t, \\ \epsilon_0(\boldsymbol{x}) = 0. \end{cases} \tag{22}$$

□

Corollary 3.2. *For any $t \in [0, 1]$, the error ϵ_t satisfies*

$$\epsilon_t(\phi_t(\boldsymbol{x})) \cdot \det \nabla \phi_t(\boldsymbol{x}) = -\int_0^t L_s(\phi_s(\boldsymbol{x})) \cdot \det \nabla \phi_s(\boldsymbol{x}) ds,$$

where $\phi_t(\boldsymbol{x})$ is the flow induced by the vector field $\boldsymbol{v}_t(\boldsymbol{x})$ in a similar way as that in equation (3), $\det \nabla \phi_t(\boldsymbol{x})$ denotes the determinant of the Jacobian matrix $\nabla \phi_t(\boldsymbol{x})$, and L_s is defined in Proposition 3.1.

Proof of Corollary 3.2. Let ϕ_t denote the flow of the vector field $\boldsymbol{v}_t$, i.e.

$$\begin{cases} \partial_t \phi_t = \boldsymbol{v}_t\big(\phi_t(\boldsymbol{x})\big), \\ \phi_0(\boldsymbol{x}) = \boldsymbol{x}. \end{cases} \tag{23}$$

Using Duhamel's formula (refer to (Seis, 2017)), we have the following formula for ϵ_t:

$$\epsilon_t\big(\phi_t(\boldsymbol{x})\big) \det \nabla \phi_t(\boldsymbol{x}) \quad = \epsilon_0(\boldsymbol{x}) + \int_0^t L_s\big(\phi_s(\boldsymbol{x})\big) \det \nabla \phi_s(\boldsymbol{x})\, ds = \int_0^t L_s\big(\phi_s(\boldsymbol{x})\big) \det \nabla \phi_s(\boldsymbol{x})\, ds \tag{24}$$

□

Theorem 3.3. *Under some common mild assumptions adopted in (Lu et al., 2022; Lipman et al., 2023; Albergo et al., 2023), the following inequality holds for any $t \in [0, 1]$:*

$$\mathrm{TV}(p_t, \hat{p}_t) \leq \frac{1}{2}\mathcal{L}_{\mathrm{DM}}(\theta). \tag{11}$$

Specifically, $p_t(\boldsymbol{x}) = \hat{p}_t(\boldsymbol{x})$ when both $\mathcal{L}_{\mathrm{DM}}$ is zero.

Proof of Theorem 3.3. Note that the total variation distance is defined as:

$$\mathrm{TV}(p_t, \hat{p}_t) = \frac{1}{2}\int \left|p_t(\boldsymbol{x}) - \hat{p}_t(\boldsymbol{x})\right| d\boldsymbol{x} = \frac{1}{2}\int \left|\epsilon_t(\boldsymbol{x})\right| d\boldsymbol{x} \tag{25}$$

Using the change of variables twice and applying the formula in Corollary 3.2, we obtain:

$$\begin{aligned}
\mathrm{TV}(p_t, \hat{p}_t) &= \frac{1}{2}\int \left|\epsilon_t(\boldsymbol{x})\right| d\boldsymbol{x} \\
&= \frac{1}{2}\int \left|\epsilon_t\big(\phi_t(\boldsymbol{x})\big)\right| d\,\phi_t(\boldsymbol{x}) \\
&= \frac{1}{2}\int \left|\epsilon_t\big(\phi_t(\boldsymbol{x})\big)\det \nabla\phi_t(\boldsymbol{x})\right| d\boldsymbol{x} \\
&= \frac{1}{2}\int \left|\int_0^t L_s\big(\phi_s(\boldsymbol{x})\big)\det \nabla\phi_s(\boldsymbol{x})\, ds\right| d\boldsymbol{x} \\
&\leq \frac{1}{2}\int\int_0^t \left|L_s\big(\phi_s(\boldsymbol{x})\big)\det \nabla\phi_s(\boldsymbol{x})\right| ds\, d\boldsymbol{x} \\
&= \frac{1}{2}\int_0^t \int \left|L_s(\boldsymbol{x})\right| d\boldsymbol{x}\, ds
\end{aligned} \tag{26}$$

Substituting the expression for L_s, we see that:

$$\begin{aligned}
2\,\mathrm{TV}(p_t, \hat{p}_t) &\leq \int_0^t \int \left|p_t\big(\nabla\cdot(\boldsymbol{u}_s - \boldsymbol{v}_s)\big) + p_s(\boldsymbol{u}_s - \boldsymbol{v}_s)\cdot\nabla\log p_s\right| d\boldsymbol{x}\, ds \\
&\leq \int_0^t \mathbb{E}_{p_s}\left|\nabla\cdot(\boldsymbol{u}_s - \boldsymbol{v}_s) + (\boldsymbol{u}_s - \boldsymbol{v}_s)\cdot\nabla\log p_s\right| ds \\
&\leq \int_0^T \mathbb{E}_{p_t}\left|\nabla\cdot(\boldsymbol{u}_t - \boldsymbol{v}_t) + (\boldsymbol{u}_t - \boldsymbol{v}_t)\cdot\nabla\log p_t\right| dt \\
&= \mathcal{L}_{\mathrm{DM}}(\theta).
\end{aligned} \tag{27}$$

This completes the proof. □

Theorem 4.1. *We have the following inequality:*

$$\mathcal{L}_{\mathrm{DM}}(\theta) \leq \mathcal{L}_{\mathrm{CDM}}(\theta). \tag{15}$$

Furthermore, we have:

$$\mathrm{TV}(p_t, \hat{p}_t) \leq \frac{1}{2}\mathcal{L}_{\mathrm{CDM}}(\theta), \tag{16}$$

for any $t \in [0, 1]$.

Proof of Theorem 4.1. From equation (13), we can show that:

$$\begin{aligned}
p_t\big(\nabla\cdot\boldsymbol{u}_t + \boldsymbol{u}_t\cdot\nabla\log p_t\big) &= \nabla\cdot\big(p_t\boldsymbol{u}_t\big) \\
&= \int \nabla\cdot\big(p_t(\boldsymbol{x}|\boldsymbol{x}_1)\boldsymbol{u}_t(\boldsymbol{x}|\boldsymbol{x}_1)\big)p(\boldsymbol{x}_1)\, d\boldsymbol{x}_1 \\
&= \int \Big(p_t(\boldsymbol{x}|\boldsymbol{x}_1)\nabla\cdot\boldsymbol{u}_t(\boldsymbol{x}|\boldsymbol{x}_1) + \boldsymbol{u}_t(\boldsymbol{x}|\boldsymbol{x}_1)\cdot\nabla p_t(\boldsymbol{x}|\boldsymbol{x}_1)\Big)p(\boldsymbol{x}_1)\, d\boldsymbol{x}_1.
\end{aligned} \tag{28}$$

On the other hand, we have

$$\begin{aligned} p_t\big(\nabla \cdot \boldsymbol{v}_t + \boldsymbol{v}_t \cdot \nabla \log p_t\big) &= p_t \nabla \cdot \boldsymbol{v}_t + \boldsymbol{v}_t \cdot \nabla p_t \\ &= \bigg(\int p_t(\boldsymbol{x}|\boldsymbol{x}_1) p(\boldsymbol{x}_1)\, d\boldsymbol{x}_1\bigg) \nabla \cdot \boldsymbol{v}_t + \boldsymbol{v}_t \cdot \nabla \bigg(\int p_t(\boldsymbol{x}|\boldsymbol{x}_1) p(\boldsymbol{x}_1)\, d\boldsymbol{x}_1\bigg) \\ &= \int \big(p_t(\boldsymbol{x}|\boldsymbol{x}_1) \nabla \cdot \boldsymbol{v}_t\big) p(\boldsymbol{x}_1)\, d\boldsymbol{x}_1 + \int \big(\boldsymbol{v}_t \cdot \nabla p_t(\boldsymbol{x}|\boldsymbol{x}_1)\big) p(\boldsymbol{x}_1)\, d\boldsymbol{x}_1 \\ &= \int \big(p_t(\boldsymbol{x}|\boldsymbol{x}_1) \nabla \cdot \boldsymbol{v}_t + \boldsymbol{v}_t \cdot \nabla p_t(\boldsymbol{x}|\boldsymbol{x}_1)\big) p(\boldsymbol{x}_1)\, d\boldsymbol{x}_1. \end{aligned} \tag{29}$$

Combining equation (28) with equation (29), we deduce that:

$$\begin{aligned} & p_t\big(\nabla \cdot \boldsymbol{u}_t + \boldsymbol{u}_t \cdot \nabla \log p_t\big) - p_t\big(\nabla \cdot \boldsymbol{v}_t + \boldsymbol{v}_t \cdot \nabla \log p_t\big) \\ &= \bigg(\int \Big(p_t(\boldsymbol{x}|\boldsymbol{x}_1) \nabla \cdot \boldsymbol{u}_t(\boldsymbol{x}|\boldsymbol{x}_1) + \boldsymbol{u}_t(\boldsymbol{x}|\boldsymbol{x}_1) \cdot \nabla p_t(\boldsymbol{x}|\boldsymbol{x}_1)\Big) p(\boldsymbol{x}_1)\, d\boldsymbol{x}_1\bigg) \\ &\qquad - \bigg(\int \big(p_t(\boldsymbol{x}|\boldsymbol{x}_1) \nabla \cdot \boldsymbol{v}_t + \boldsymbol{v}_t \cdot \nabla p_t(\boldsymbol{x}|\boldsymbol{x}_1)\big) p(\boldsymbol{x}_1)\, d\boldsymbol{x}_1\bigg) \\ &= \int \big(\nabla \cdot \boldsymbol{u}_t(\boldsymbol{x}|\boldsymbol{x}_1) - \nabla \cdot \boldsymbol{v}_t\big) p_t(\boldsymbol{x}|\boldsymbol{x}_1) p(\boldsymbol{x}_1)\, d\boldsymbol{x}_1 + \int \big(\boldsymbol{u}_t(\boldsymbol{x}|\boldsymbol{x}_1) - \boldsymbol{v}_t(\boldsymbol{x})\big) \cdot \nabla p_t(\boldsymbol{x}|\boldsymbol{x}_1) p(\boldsymbol{x}_1)\, d\boldsymbol{x}_1 \\ &= \int \bigg[\big(\nabla \cdot \boldsymbol{u}_t(\boldsymbol{x}|\boldsymbol{x}_1) - \nabla \cdot \boldsymbol{v}_t\big) + \Big(\boldsymbol{u}_t(\boldsymbol{x}|\boldsymbol{x}_1) - \boldsymbol{v}_t(\boldsymbol{x})\Big) \cdot \nabla \log p_t(\boldsymbol{x}|\boldsymbol{x}_1)\bigg] p_t(\boldsymbol{x}|\boldsymbol{x}_1) p(\boldsymbol{x}_1)\, d\boldsymbol{x}_1. \end{aligned} \tag{30}$$

Now from the definitions of $\mathcal{L}_{\mathrm{DM}}(\theta)$ and $\mathcal{L}_{\mathrm{CDM}}(\theta)$, we deduce that

$$\begin{aligned} \mathcal{L}_{\mathrm{DM}}(\theta) &= \int_0^T \int p_t \Big|\nabla \cdot (\boldsymbol{u}_t - \boldsymbol{v}_t) + (\boldsymbol{u}_t - \boldsymbol{v}_t) \cdot \nabla \log p_t\Big|\, d\boldsymbol{x}\, dt \\ &= \int_0^T \int \Big|p_t\big(\nabla \cdot \boldsymbol{u}_t + \boldsymbol{u}_t \cdot \nabla \log p_t\big) - p_t\big(\nabla \cdot \boldsymbol{v}_t + \boldsymbol{v}_t \cdot \nabla \log p_t\big)\Big|\, d\boldsymbol{x}\, dt \\ &= \int_0^T \int \bigg|\int \bigg[\big(\nabla \cdot \boldsymbol{u}_t(\boldsymbol{x}|\boldsymbol{x}_1) - \nabla \cdot \boldsymbol{v}_t\big) + \Big(\boldsymbol{u}_t(\boldsymbol{x}|\boldsymbol{x}_1) - \boldsymbol{v}_t(\boldsymbol{x})\Big) \cdot \nabla \log p_t(\boldsymbol{x}|\boldsymbol{x}_1)\bigg] p_t(\boldsymbol{x}|\boldsymbol{x}_1) p(\boldsymbol{x}_1)\, d\boldsymbol{x}_1\bigg|\, d\boldsymbol{x}\, dt \\ &\leq \int_0^T \int \int \Big|\big(\nabla \cdot \boldsymbol{u}_t(\boldsymbol{x}|\boldsymbol{x}_1) - \nabla \cdot \boldsymbol{v}_t\big) + \Big(\boldsymbol{u}_t(\boldsymbol{x}|\boldsymbol{x}_1) - \boldsymbol{v}_t(\boldsymbol{x})\Big) \cdot \nabla \log p_t(\boldsymbol{x}|\boldsymbol{x}_1)\Big| p_t(\boldsymbol{x}|\boldsymbol{x}_1) p(\boldsymbol{x}_1)\, d\boldsymbol{x}_1\, d\boldsymbol{x}\, dt \\ &= \mathcal{L}_{\mathrm{CDM}}(\theta). \end{aligned} \tag{31}$$

□

B. Experiments Details

B.1. Trajectory Sampling for Dynamical Systems

For this experiment, we repeatedly use the Dormand-Prince ODE solver with an absolute tolerance 1.4×10^{-8} and relative tolerance 1×10^{-6}.

Lorenz The Lorenz system (Lorenz, 1963) is a chaotic dynamical system given by

$$\dot{\boldsymbol{x}} = \begin{bmatrix} \dot{x}_1 \\ \dot{x}_2 \\ \dot{x}_3 \end{bmatrix} = F(\boldsymbol{x}) = \begin{bmatrix} \sigma(x_2 - x_1) \\ x_1(\rho - x_3) - x_2 \\ x_1 x_2 - \beta x_3 \end{bmatrix}$$

Following (Finzi et al., 2023), we set $\sigma = 10$, $\rho = 28$ and $\beta = 8/3$, and we used a scaled version of the Lorenz system to bound the system components to $[-3, 3]$ for $i \in 1, 2, 3$ while preserving the original dynamics. The scaled system is given by $\tilde{F}(\boldsymbol{x}) = F(20\boldsymbol{x})/20$.

FitzHugh-Nagumo The FitzHugh-Nagumo system (FitzHugh, 1961; Nagumo et al., 1962) is a dynamical system modeling an excitable neuron and is given by

$$\dot{x}_i = x_i(a_i - x_i)(x_i - 1) - y_i + k\sum_{j=1}^{d} A_{ij}(x_j - x_i)$$
$$\dot{y}_i = b_i x_i - c_i y_i$$

for $i \in \{1, 2\}$. Following (Farazmand & Sapsis, 2019; Finzi et al., 2023), the parameters are set as follows: $a_1 = a_2 = -0.025794$, $b_1 = 0.0065$, $b_2 = 0.0135$, $c_1 = c_2 = 0.2$, $k = 0.128$, and $A_{ij} = 1 - \delta_{ij}$ where δ is the Kronecker delta.

Trajectory dataset construction Trajectories for the dataset are computed using the ODE solver. The trajectories' initial conditions are sampled from Gaussian distributions – $\mathcal{N}(\mathbf{0}, \boldsymbol{I})$ for Lorenz, and $\mathcal{N}(\mathbf{0}, (0.2)^2\boldsymbol{I})$ for FitzHugh-Nagumo. Each trajectory has 60 consecutive and evenly spaced time steps, where the first time step occurs after some trajectory "burn-in" time to allow the system to reach its stationary trajectory distribution. The first 30 and 250 time steps computed by the ODE solver are "burn-in" for Lorenz and FitzHugh-Nagumo, respectively. The time step sizes are 0.1 and 6.0, respectively.

Model hyperparameters and training All the models used the same UNet architecture as in (Finzi et al., 2023), and we used a variance exploding schedule (Song et al., 2020). We train the models on a training set of 32,000 trajectories computed by the ODE solver using Adam for 2,000 epochs with a batch size of 500. For FM and FDM, we also used an exponential decay learning rate scheduler with a decay rate of 0.995. The initial learning rate for the diffusion model and FM was 10^{-4}. The learning rate and regularization coefficients for FDM were tuned using Optuna (Akiba et al., 2019) for the lowest CFM loss produced by the EMA parameters and are given in Table 10. We sampled the times for the diffusion and CFM loss on a shifted grid following (Finzi et al., 2023).

Dynamical system	Learning rate	λ_1	λ_2
Lorenz	0.000796	1	0.000385
FitzHugh-Nagumo	0.000245	1	0.00552

Table 10. Learning rate and regularization coefficient used to train FDM for Lorenz and FitzHugh-Nagumo dynamical systems.

We evaluated the models with the exponential moving average (EMA) of the parameters with a 2,000 epoch period.

Loss weighting functions The loss of the diffusion model is equation (7) of (Song et al., 2020) where we used $\lambda(t) = \sigma_t^2$ as the weighting. For both FM and FDM, the term $\mathcal{L}_{\text{CFM}}$ in their loss was weighted by $1/(\sigma'_{1-t})^2$. The term $\mathcal{L}_{\text{CDM}}$ in the loss of FDM was weighted by $\sigma_{1-t}/(\sigma'_{1-t}Md)$ where $M = 60$ is the number of trajectory time steps and d is the dimension of the dynamical system.

Estimating the divergence We estimated the divergence of FDM with respect to its trajectory input using the Hutchinson tracer estimator (Hutchinson, 1989; Grathwohl et al., 2018) where the noise vector is sampled from $\mathcal{N}(\mathbf{0}, \boldsymbol{I})$.

Likelihood estimation We computed a test set of 32,000 trajectories using the ODE solver and evaluated their log-likelihood using the continuous change-of-variables formula from (Grathwohl et al., 2018) with the ODE solver. Table 6 was produced by computing the mean log-likelihood over the trajectories and their dimension.

B.2. DNA Sequence Generation

In this task, the model approximates a classifier

$$\hat{p}(\boldsymbol{x}_1|\boldsymbol{x}, \theta) \approx \frac{p_t(\boldsymbol{x}|\boldsymbol{x}_1)p(\boldsymbol{x}_1)}{p_t(\boldsymbol{x})} \tag{32}$$

instead of directly approximating the vector field $\hat{\boldsymbol{v}}_t(\boldsymbol{x}, \theta) \approx \boldsymbol{u}_t(\boldsymbol{x})$. Then, it constructs a vector field based on the classifier as follows:

$$\hat{\boldsymbol{v}}_t(\boldsymbol{x}, \theta) = \sum_{i=1}^{K} \boldsymbol{u}_t(\boldsymbol{x}|\boldsymbol{x}_1 = \boldsymbol{e}_i)\hat{p}(\boldsymbol{x}_1 = \boldsymbol{e}_i|\boldsymbol{x}, \theta), \tag{33}$$

where K is the number of categories and the divergence term is given by

$$\nabla_{\boldsymbol{x}} \cdot \hat{\boldsymbol{v}}_t(\boldsymbol{x}, \theta) = \sum_{i=1}^{K} \left[\left\langle \nabla p(\boldsymbol{x}_1 = \boldsymbol{e}_i | \boldsymbol{x}, \theta), \boldsymbol{u}_t(\boldsymbol{x} | \boldsymbol{x}_1 = \boldsymbol{e}_i) \right\rangle + p(\boldsymbol{x}_1 = \boldsymbol{e}_i | \boldsymbol{x}, \theta) \nabla_{\boldsymbol{x}} \cdot \boldsymbol{u}_t(\boldsymbol{x} | \boldsymbol{x}_1 = \boldsymbol{e}_i) \right] \tag{34}$$

If we directly learn $\nabla_{\boldsymbol{x}} \cdot \hat{\boldsymbol{v}}_t(\boldsymbol{x}, \theta)$, it requires computing $\nabla_{\boldsymbol{x}} \cdot \left[\boldsymbol{u}_t(\boldsymbol{x} | \boldsymbol{x}_1 = \boldsymbol{e}_i) \hat{p}(\boldsymbol{x}_1 = \boldsymbol{e}_i | \boldsymbol{x}, \theta) \right]$ for $i = 1, 2, ..., K$ which can be very expensive in memory footprint and time consumption. Furthermore, notice that $\boldsymbol{u}_t(\boldsymbol{x} | \boldsymbol{x}_1 = \boldsymbol{e}_i)$ is a pre-defined vector field that is independent of parameters θ and so is $\nabla_{\boldsymbol{x}} \cdot \boldsymbol{u}_t(\boldsymbol{x} | \boldsymbol{x}_1 = \boldsymbol{e}_i)$. Thus, there is no need to learn it.

For $p(\boldsymbol{x}_1 = \boldsymbol{e}_i | \boldsymbol{x}, \theta)$, Appendix A of (Stark et al., 2024) states that $\hat{\boldsymbol{v}}_t(\boldsymbol{x}, \theta)$ approximates the vector field if $\hat{p}(\boldsymbol{x}_1 | \boldsymbol{x}, \theta)$ ideally approximates the classifier $p(\boldsymbol{x}_1 | \boldsymbol{x})$. Consider an ideal classifier $p(\boldsymbol{x}_1 = \boldsymbol{e}_i | \boldsymbol{x})$ for class $\boldsymbol{x}_1 = \boldsymbol{e}_i$, then $p(\boldsymbol{x}_1 = \boldsymbol{e}_i | \boldsymbol{x}) = 1$ if $\boldsymbol{x}$ belongs to class $\boldsymbol{x}_1$ else 0. Let $\boldsymbol{x} \in D$, where D is the domain of this classifier, then we have

- $p(\boldsymbol{x}_1 = \boldsymbol{e}_i | \boldsymbol{x})$ is not continuous in D.
- Suppose D_1 is the union of all the differentiable sub-domains of D, then $\nabla_{\boldsymbol{x}} p(\boldsymbol{x}_1 = \boldsymbol{e}_i | \boldsymbol{x}) = \mathbf{0}$ for $\boldsymbol{x} \in D_1$.

Therefore, the remaining thing is to include $\|\nabla_{\boldsymbol{x}} p(\boldsymbol{x}_1 = \boldsymbol{e}_i | \boldsymbol{x})\|$ for $\boldsymbol{x} \in D_1$ in the training objective. In practice, we train the classifier by empirically estimating the cross entropy based on the perturbed points $\boldsymbol{x}$ with its corresponding initial data $\boldsymbol{x}_1$ as the class label. We can just assume any point in a sufficient small ball around such a perturbed data point $\boldsymbol{x}$ belongs to the same class $\boldsymbol{x}_1$ so the classifier is differentiable inside this small ball, then we penalize $\|\nabla_{\boldsymbol{x}} \hat{p}(\boldsymbol{x}_1 | \boldsymbol{x}, \theta)\|$ in training the model.

Promoter Data We use a dataset of 100,000 promoter sequences with 1,024 base pairs extracted from a database of human promoters (Hon et al., 2017). Each sequence has a CAGE signal (Shiraki et al., 2003) annotation available from the FANTOM5 promoter atlas, which indicates the likelihood of transcription initiation at each base pair. Sequences from chromosomes 8 and 9 are used as a test set, and the rest for training.

Model hyperparameters and training We just follow the experimental setup of (Stark et al., 2024). For the simplex dimension toy experiment, we train all models for 450,000 steps with a batch size of 512 to ensure that they have all converged and then evaluate the KL of the final step. For promoter design, we train for 200 epochs with a learning rate of 5×10^{-4} and early stopping on the MSE on the validation set. We use 100 inference steps for generation. Table 11 show how we set λ_1 and λ_2 for divergence loss.

Tasks	Learning rate	λ_1	λ_2
Simplex Dimension	5×10^{-4}	0.5	0.05
Promoter Design	5×10^{-4}	1	0.01

Table 11. Learning rate and regularization coefficient used to train FDM for DNA sequence.

B.3. Generative Modeling for Videos

We follow the experimental setting and models used in (Davtyan et al., 2023).

Architechture We use U-ViT (Bao et al., 2023) to model the flow matching vector field and use VQGAN (Esser et al., 2021) to encode (resp. decode) each frame of the video to (resp. from) the latent space with the following configurations

Training Setup See table B.3.

C. Additional numerical results

C.1. Dirichlet Flow Matching

Table 14 shows the test KL divergence of models for the simplex dimension toy experiment of DNA sequence generation.

Parameter	**KTH**	**BAIR**
embed_dim	4	4
n_embed	16384	16384
double_z	False	False
z_channels	4	4
resolution	64	64
in_channels	3	3
out_ch	3	3
ch	128	128
ch_mult	[1,2,2,4]	[1,2,2,4]
num_res_blocks	2	2
attn_resolutions	[16]	[16]
dropout	0.0	0.0
disc_conditional	False	False
disc_in_channels	3	3
disc_start	20k	20k
disc_weight	0.8	0.8
codebook_weight	1.0	1.0

Table 12. Parameters of VQGAN for the KTH dataset.

Hyperparameter	Values/Search Space
Iterations	300000
Batch size	[16, 32, 64]
Learning rate	[2e-4, 2e-5]
Learning rate scheduler	polynomial
Learning rate decay power	0.5
Weight decay rate	1e-12
λ_1, λ_2	[[0.5, 1e-2], [1, 1e-2]]

Table 13. Training hyperparameters of video prediction.

Method	KL Divergence
Linear FM	$2.5_{\pm 0.1}$E-2
Linear FDM	$2.1_{\pm 0.1}$E-2
Dirichlet FM	$1.8_{\pm 0.1}$E-2
Dirichlet FDM	$1.5_{\pm 0.1}$E-2

Table 14. KL divergence of the generated distribution to the target distribution.

C.2. Flow matching for user-defined events

Unguided sampling histograms: The histograms of the event constraint values for the trajectories sampled without guidance by each model are shown in Fig. 7.

KL Divergence Table 7 shows the KL divergence between the histogram distributions. For Lorenz, FDM's unguided sampling has the lowest KL divergence, with the divergence of the diffusion model and FM being 0.0007 and 0.0032 larger. In guided sampling, the FM has a lower KL divergence than the diffusion model and FDM by about 0.02 and 0.05, respectively. For FitzHugh-Nagumo, the diffusion model has a lower KL divergence than FM and FDM by 0.002. In guided sampling, FDM attains the largest performance gap with a KL divergence of about 0.1 and 0.14 lower than the diffusion model and FM, respectively.

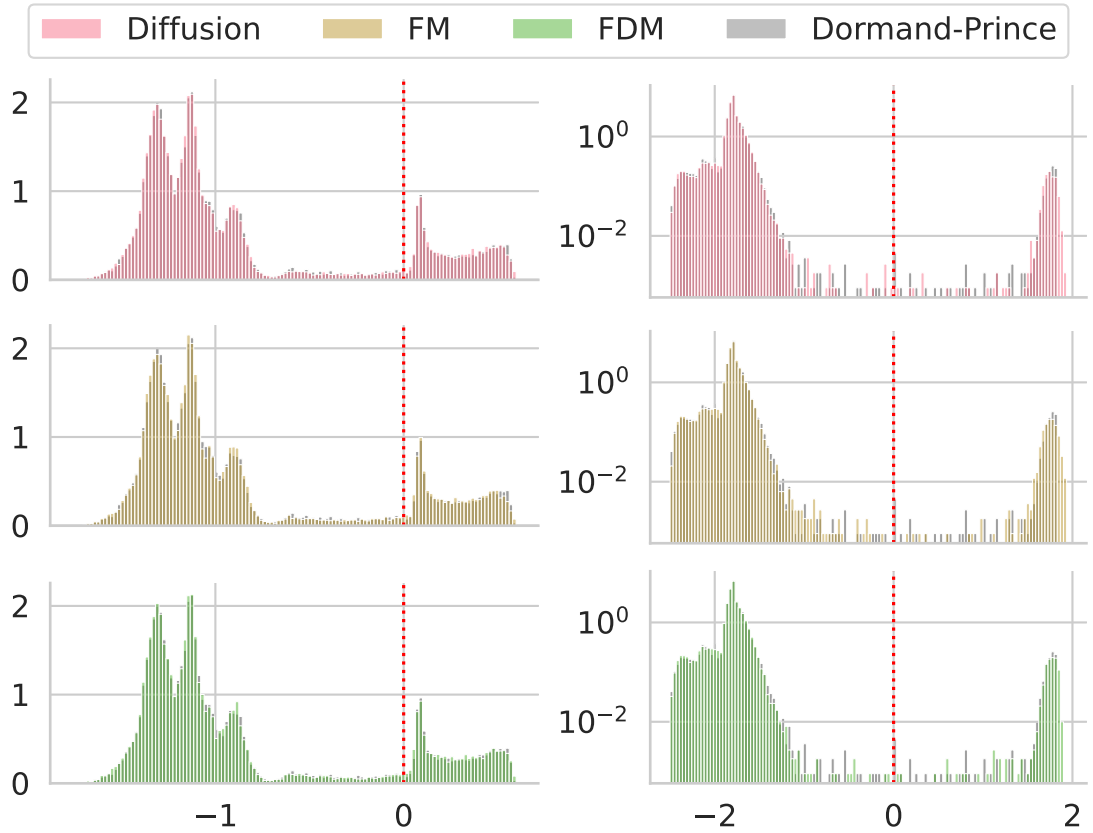

(a) Lorenz (b) FitzHugh-Nagumo

Figure 7. Histograms of the event constraint C evaluated on the data and trajectories generated from the models.

	Lorenz		FitzHugh-Nagumo	
Model	$p(\boldsymbol{x}_1)$	$p(\boldsymbol{x}_1\|E)$	$p(\boldsymbol{x}_1)$	$p(\boldsymbol{x}_1\|E)$
Diffusion	0.0056	0.2774	0.0260	0.3011
FM	0.0081	0.2560	0.0280	0.3468
FDM	0.0049	0.3045	0.0280	0.2084

Table 15. KL divergence between the histograms of the event constraint value $C(\boldsymbol{x}_1)$ for event trajectories $\boldsymbol{x}_1$ in the dataset of trajectories computed by an ODE solver and event trajectories sampled with event guidance from the models.

D. Squared Loss

We observe that the conditional divergence loss in equation (14) is an absolute-value objective, whose non-differentiability at the origin removes smoothness and can be less efficient than squared-error alternatives. In practice, we replace it with the following squared loss:

$$\mathcal{L}_{\text{CDM-2}}(\theta) = \mathbb{E}_{t,p_t(\boldsymbol{x}|\boldsymbol{x}_1),p(\boldsymbol{x}_1)}\Big[\Big(\big(\nabla\cdot\boldsymbol{u}_t(\boldsymbol{x}|\boldsymbol{x}_1) - \nabla\cdot\boldsymbol{v}_t(\boldsymbol{x},\theta)\big) + \big(\boldsymbol{u}_t(\boldsymbol{x}|\boldsymbol{x}_1) - \boldsymbol{v}_t(\boldsymbol{x},\theta)\big)\cdot\nabla\log p_t(\boldsymbol{x}|\boldsymbol{x}_1)\Big)^2\Big], \quad (35)$$

where sg denotes 'stop gradient'—a technique used to prevent certain parts of a computational graph from contributing to the gradient computation during backpropagation. To decouple the objectives during training, we insert a stop-gradient operation so that the CFM term governs the vector-regressor discrepancy while the CDM term targets only the divergence term. Empirically, stopping the gradient of $\boldsymbol{v}_t(\boldsymbol{x};\theta)$ inside the CDM leads to noticeably faster and more stable convergence.

Theorem D.1 (Upper Bound)**.** *The squared loss $\mathcal{L}_{\text{CDM-2}}(\theta)$ provides an upper bound:*

$$\mathcal{L}_{\text{CDM}}(\theta) \le \sqrt{\mathcal{L}_{\text{CDM-2}}(\theta)} \quad (36)$$

Proof. Let

$$f(\boldsymbol{x}, \boldsymbol{x}_1, t) = \big(\nabla \cdot \boldsymbol{u}_t(\boldsymbol{x}|\boldsymbol{x}_1) - \nabla \cdot \boldsymbol{v}_t(\boldsymbol{x}, \theta)\big) + \big(\boldsymbol{u}_t(\boldsymbol{x}|\boldsymbol{x}_1) - \boldsymbol{v}_t(\boldsymbol{x}, \theta)\big) \cdot \nabla \log p_t(\boldsymbol{x}|\boldsymbol{x}_1)$$

we have

$$\begin{aligned}
\mathcal{L}_{\mathrm{CDM}}(\theta) &= \int\int\int |f(\boldsymbol{x}, \boldsymbol{x}_1, t)| p_t(\boldsymbol{x}|\boldsymbol{x}_1) p(\boldsymbol{x}_1) d\boldsymbol{x} d\boldsymbol{x}_1 dt \\
&= \int\int\int |f(\boldsymbol{x}, \boldsymbol{x}_1, t)| p(\boldsymbol{x}|\boldsymbol{x}_1, t) p(\boldsymbol{x}_1) p(t) d\boldsymbol{x} d\boldsymbol{x}_1 dt \\
&\underbrace{\leq}_{\text{Cauchy-Schwarz Ineq.}} \Big(\int\int\int f^2(\boldsymbol{x}, \boldsymbol{x}_1, t) p(\boldsymbol{x}|\boldsymbol{x}_1, t) p(\boldsymbol{x}) p(t) d\boldsymbol{x} d\boldsymbol{x}_1 dt\Big)^{\frac{1}{2}} \\
&= \sqrt{\mathcal{L}_{\text{CDM-2}}(\theta)}
\end{aligned} \tag{37}$$

where we define $p_t(\boldsymbol{x}|\boldsymbol{x}_1) := p(\boldsymbol{x}|\boldsymbol{x}_1, t)p(t)$. □

In practice, a stop-gradient operation is applied on the $\boldsymbol{v}_t(\boldsymbol{x}, \theta)$ in $\mathcal{L}_{\text{CDM-2}}(\theta)$ following common practice (Frans et al., 2024; Lu et al., 2022; Song & Dhariwal, 2023). In our case, we train the model by combining $\mathcal{L}_{\mathrm{CFM}}(\theta)$ and $\mathcal{L}_{\text{CDM-2}}(\theta)$ so the stop-gradient operation eliminates the need for "double backpropagation" through $\boldsymbol{v}_t(\boldsymbol{x}, \theta)$, making the training more efficient.